



Cite this: *New J. Chem.*, 2024, 48, 14071

# Effect of the extended $\pi$ -surface and *N*-butyl substituents of imidazoles on their reactivity, electrochemical behaviours and biological interactions of corresponding Pt(II)-CNC carbene complexes: exploring DFT and docking interactions†

Rajesh Bellam,<sup>a</sup> Daniel O. Onunga,<sup>c</sup> Deogratius Jaganyi,<sup>de</sup> Ross Robinson<sup>a</sup> and Allen Mambanda<sup>a</sup>

In this study, we synthesised and characterised three C<sup>^</sup>N<sup>^</sup>C pincer (N-heterocyclic carbene)-type tridentate ligands, namely, 2,6-bis[(3-methylimidazolium-1-yl)methyl]pyridine dibromide (**L**<sub>1</sub>), 2,6-bis[(3-methylbenzimidazolium-1-yl)methyl]pyridine dibromide (**L**<sub>2</sub>) and 2,6-bis[(3-butylimidazolium-1-yl)methyl]pyridine dibromide (**L**<sub>3</sub>), and their corresponding six-membered chelates with Pt(II) to form **PtL**<sub>1</sub>–**PtL**<sub>3</sub> complexes, namely, 2,6-bis[(3-methylimidazolium-1-yl)methyl]pyridinechloroplatinum(II) tetrafluoroborate (**PtL**<sub>1</sub>), 2,6-bis[(3-methylbenzimidazol-1-yl)methyl]pyridinechloroplatinum(II) tetrafluoroborate (**PtL**<sub>2</sub>) and 2,6-bis[(3-butylimidazol-1-yl)methyl]pyridinechloroplatinum(II) tetrafluoroborate (**PtL**<sub>3</sub>). Substitution kinetics using thiourea nucleophiles (tu, dmtu and tmtu), structural properties through theoretical DFT, biological interactions with DNA/BSA, electrochemical behaviors using cyclic voltammetry and docking simulations for Pt(II) C<sup>^</sup>N<sup>^</sup>C pincer complexes were investigated. The extended  $\pi$  surface of benzimidazole (**PtL**<sub>2</sub>) caused  $\sigma$ -donation in *cis*-Pt–C bonds, while *N*-butyl arms (**PtL**<sub>3</sub>) on the bis(3-methylimidazolium-1-yl)pyridine C<sup>^</sup>N<sup>^</sup>C pincer ligand had a steric influence on the labile ligand, leading to an increasing order of chloride substitution as follows: **PtL**<sub>3</sub> < **PtL**<sub>2</sub> < **PtL**<sub>1</sub>. The nucleophile's reactivity order is in accordance with its bulkiness, and the order is tu > dmtu > tmtu. Reactivity trends were justified by the trends in theoretical DFT data. Strong *cis*  $\sigma$ -donor ligands prevent the co-ordination of the spectator ligand. Large negative entropy of activation ( $\Delta S^\ddagger$ ) and positive enthalpy of activation ( $\Delta H^\ddagger$ ) support a limiting associative substitution mechanism. Biological interactions of **PtL**<sub>1</sub>–**PtL**<sub>3</sub> with CT-DNA and BSA complexes were confirmed using spectroscopic and cyclic voltammetry (CV) titrations, and the data obtained established moderate-to-strong binding affinities. Complexes bind to CT-DNA mainly via the groove mode and to a lesser extent via intercalation, whereas they insert into the upper protein cleft of BSA. Electrochemistry results also established the groove binding mode of interaction, and  $-\Delta G$  values affirmed the binding process as spontaneous. Molecular docking simulations of **PtL**<sub>1</sub>–**PtL**<sub>3</sub> with CT-DNA and BSA corroborated with groove binding being the main binding mode.

Received 1st February 2024,  
Accepted 4th July 2024

DOI: 10.1039/d4nj00552j

rsc.li/njc

<sup>a</sup> School of Chemistry and Physics, University of KwaZulu-Natal, Private Bag X01, Scottsville, Pietermaritzburg 3209, South Africa.  
E-mail: rajeshchowdarybellam@gmail.com

<sup>b</sup> Department of Chemistry, Medi-Caps University, A. B. Road, Pigdambar, Rau, Indore 453331, Madhya Pradesh, India

<sup>c</sup> Department of Chemistry, Maseno University, P.O. Box 333-40105, Maseno, Kenya

<sup>d</sup> School of Pure and Applied Sciences, Mount Kenya University, P.O. Box 342-01000, Thika, Kenya

<sup>e</sup> Department of Chemistry, Durban University of Technology, P.O. Box 1334, Durban 4000, South Africa

† Electronic supplementary information (ESI) available. See DOI: <https://doi.org/10.1039/d4nj00552j>

## Introduction

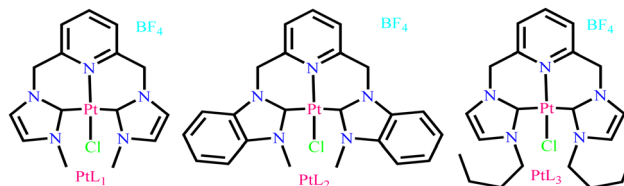
Stability, chemical reactivity and biological activities of transition metal complexes are greatly influenced by coordinated ligands, particularly chelated ones. Among the innumerable (di-, tri-, and tetra-) types of chelating ligands for coordinating d<sup>8</sup> metal ions, tridentate pincer ligands form symmetric di-chelated square complexes characterized by high thermodynamic stability and moderate-to-high reactivity depending on the degree of  $\pi$ -conjugation, type of chelation and metal ions. A good balance between the reactivity and stability of square-planar complexes as espoused by electronic and steric properties of pincer ligands (*e.g.*



the donor properties of the coordinated moiety, the position and nature of the donor atom, the size of the chelation ring, and the steric demands or bulk of the moieties within tridentate ligands) ensures the versatility in their applications. There is a large collection of symmetrical pincer ligands that include bis(phosphinite)s, bis(phosphonimine)s, bis(thioether)s, bis(N-heterocyclic)carbenes, and bis(NHC)s.<sup>1,2</sup> Pincer bis(NHC)s of the (C<sup>^</sup>N/C<sup>^</sup>C) type have been known since 1968.<sup>3–5</sup> These azolium ligands form cyclometalated transition metal complexes with remarkable stability in the presence of oxygen, moisture, and heat and are easily fine-tuned to achieve optimum physicochemical properties and reactivity for various applications.

The most common C<sup>^</sup>N/C<sup>^</sup>N<sup>^</sup>C ligands are precipitated as diazolium bromides, which have to undergo C–H-activated deprotonation at the bis(imidazolium, pyridinium, pyrazolium, benzimidazolium, triazolium, tetrazolium, and thiazolium) carbons before coordinating to metal ions. A neutral N or a carbene C (sp<sup>2</sup>)-bridgehead atom together with two other carbene atoms (in lateral positions) forms the usual donor set of pincer bis(NHC) tridentates. The ligands are regarded as good *cis*- $\sigma$ -donor ligands with relatively poor  $\pi$ -accepting ability.<sup>6–9</sup> Consequently, they form a variety of air/moisture and thermally stable mono and di nuclear complexes with many transition metal ions.<sup>10,11</sup> Non-conjugated C<sup>^</sup>N<sup>^</sup>C ligands are mainly  $\sigma$ -donors (C<sup>^</sup>N<sup>^</sup>C-to-metal ( $\sigma \rightarrow d$ ) donation), whereas those containing conjugated donor rings such as the benzimidazole or indazolium are mixed  $\sigma/\pi$  donors and may show strong C<sup>^</sup>N<sup>^</sup>C-to-metal ( $\pi \rightarrow d$ ) and moderate metal-to-C<sup>^</sup>N<sup>^</sup>C ( $d \rightarrow \pi^*$ ) back donation of electron charge transfers.<sup>12</sup> Thus, research efforts are geared towards the synthesis of C<sup>^</sup>N/C<sup>^</sup>N<sup>^</sup>C-stabilized Pt/Pd(II) complexes that offer structural and functional diversities and allow systematic evaluation of the structure–reactivity/activity to judiciously develop application-apt d<sup>8</sup>-complexes.

Square-planar Pt(II) complexes have attracted considerable research attention in various scientific fields that include catalysis, materials science and bio-medicinal chemistry. The anticancer activity of *cis*-platin became the pinnacle of the search for more oncological drugs of better efficacy. One of the strategies has been to tune the activity of the Pt(II) analogs by varying the steric and electronic properties of the ligands around the Pt(II) ion. The cationic bis(NHC)s (C<sup>^</sup>N<sup>^</sup>C) ligands have not been explored to a greater extent in this regard despite the strong  $\sigma$ -donating property of their bis(carbene), which can form strong metal–carbon  $\sigma$ -bonds. Those Pt(II) C<sup>^</sup>N<sup>^</sup>C complexes are thermodynamically stable and of tuneable reactivity and biological activity.<sup>13</sup> Such complexes are hypothesised to bind strongly to the DNA helix, inducing cellular regulatory processes some of which form part of the postulated mechanisms for the anti-proliferative activity of metal–drugs. Pt(II) C<sup>^</sup>N<sup>^</sup>C complexes can serve as DNA cleavage reagents, hence making them multifaceted anticancer agents.<sup>14</sup> However, not much has been done to measure the rate of substitution and mechanism of interaction of bis(carbene) Pt(II) complexes with biological anticancer targets. In this study, Pt(II) C<sup>^</sup>N<sup>^</sup>C complexes (**PtL<sub>1</sub>**–**PtL<sub>3</sub>**) bearing ligands of variable electronic and steric properties were synthesized and characterized and their rates of chloride substitution with



Scheme 1 Structural formulae of **PtL<sub>1</sub>**–**PtL<sub>3</sub>**.

S-donor bio-relevant thiourea nucleophiles (tu, dmtu and tmtu) measured to understand their reactivity with potential biological targets for a therapeutic effect. The S-nucleophiles exhibit good aqueous solubility, neutral character, robust steric demands, and high nucleophilicity.<sup>15</sup> Moreover, one of these nucleophiles has been used as a protecting agent co-administered with cisplatin to minimize the latter's acute nephrotoxicity. The synthesized complexes, **PtL<sub>1</sub>**–**PtL<sub>3</sub>** enabled a qualitative structure–reactivity relationship assessment as the extended phenyl rings and *cis*-positioned butyl arms of the carbenic donors of the imidazole rings within the coordinated tridentates are varied (Scheme 1). While the strong  $\sigma$ -donation ability of C<sup>^</sup>N<sup>^</sup>Cs is well documented, a similar understanding of their  $\pi$ -accepting ability and steric influences on their reactivity and biological interactions are not well understood, and this became our inquest to unravel.

## Experimental

### Reagents and materials

Sigma-Aldrich provided all of the reagents, which were used without further purification. Synthetic manipulations were carried out in an oxygen-free environment. Sigma-Aldrich supplied solvents (methanol, ethanol, dimethyl formamide, acetonitrile, dimethyl sulphoxide, diethyl ether, and acetone) that were dried and distilled before use. 2,6-Bis-(bromomethyl)pyridine (98%), 1-methylimidazole ( $\geq 99\%$ ), 1-methylbenzimidazole (99%), 1-butylimidazole (98%), silver(I) oxide ( $\geq 99.99\%$ ), potassium tetrachloroplatinate(II) ( $\geq 99.9\%$ ), silver tetrafluoroborate (98%), sodium perchlorate monohydrate (98%), lithium chloride ( $\geq 99\%$ ) and thiourea nucleophiles, namely, thiourea (tu,  $\geq 99.0\%$ ), 1,3-dimethyl-2-thiourea (dmtu, 99%) and 1,1,3,3-tetramethyl-2-thiourea (tmtu, 98%) were obtained from Sigma-Aldrich and used without further purification. The ligands **L<sub>1</sub>**–**L<sub>3</sub>** and their respective complexes **PtL<sub>1</sub>**–**PtL<sub>3</sub>** were synthesized according to the literature.<sup>16</sup>

### Instrumentation and characterization

The synthesized ligands and their corresponding Pt(II) C<sup>^</sup>N<sup>^</sup>C pincer complexes were characterized by several analytic techniques. Mass data were obtained using a Waters TOF Micro-mass LCT premier spectrometer operated in the positive ion mode. The spectra are presented in the electronic ESI<sup>†</sup> NMR data were obtained using a Bruker Avance DPX 400 spectrometer at a frequency of 400 MHz using either a 5-mm BBOZ probe or a 5-mm TBIZ probe at 30 °C. The elemental composition of the complexes was determined using a Thermo Scientific Flash 2000 CHNS/O Analyser. Kinetic measurements were recorded using a Varian Cary 100 Bio UV-visible spectrophotometer



coupled to a Varian Peltier temperature controller having an accuracy of  $\pm 0.05$  °C and an Applied Photophysics SX 20 stopped-flow reaction analyzer coupled to an online data acquisition system. The temperature of the instrument was controlled to be within  $\pm 0.1$  °C.

### Synthesis of imidazolium ligand salts $L_1$ – $L_3$ and corresponding Pt(II) C<sup>N</sup>C pincer complexes $PtL_1$ – $PtL_3$

Diazolium ligands 2,6-bis[(3-methylimidazolium-1-yl)methyl]pyridine dibromide ( $L_1$ ), 2,6-bis[(3-methylbenzimidazolium-1-yl)methyl]pyridine dibromide ( $L_2$ ) and 2,6-bis[(3-butylimidazolium-1-yl)methyl]pyridine dibromide ( $L_3$ ) were prepared according to a published procedure with slight modification.<sup>16</sup> In brief, 1-methylimidazole (2.87 g, 35 mmol)/1-methylbenzimidazole (4.63 g, 35 mmol)/1-butylimidazole (4.35 g, 35 mmol) in acetonitrile (10 mL) were added dropwise to a stirring solution of 2,6-bis-(bromomethyl)pyridine (3.97 g, 15 mmol) in acetonitrile (20 mL) for 1 hour under a  $N_2$  atmosphere. After 5 hours of heating at reflux under  $N_2$ , a white precipitate began to form. The reaction was continued up to 24 hours thereafter, and the precipitate was cooled to room temperature, filtered, and washed with acetonitrile and diethyl ether sequentially. After drying under a vacuum, the desired product was obtained. The results of the  $^1H$  NMR spectra, ESI<sup>+</sup> TOF MS and elemental analysis results are shown below, and the spectra of  $^1H$  NMR and TOF MS are shown in ESI,<sup>†</sup> Fig. S1–S3 and S4–S6, respectively.

**$L_1$ .** White solid powder, yield: 5.65 g, 82.7%. TOF-(ESI<sup>+</sup>)-MS,  $m/z$ : 428 ( $[M^+]$ , 100%), 268 ( $[M^+-Br]$ , 58%).  $^1H$  NMR (400 MHz, DMSO- $d_6$ ):  $\delta$  = 7.95 (t, 1H), 7.48 (d, 3H), 7.46 (s, 1H), 7.43 (d, 2H), 5.50 (s, 4H), 3.92 (s, 6H). Anal. calc. for  $C_{15}H_{19}N_5Br_2$ : C, 41.98; H, 4.46; N, 16.37. Found: C, 42.24; H, 4.29; N, 15.98.

**$L_2$ .** Off-white powder, yield: 6.64 g, 77.3%. TOF-(ESI<sup>+</sup>)-MS,  $m/z$ : 436 ( $[M^+-Br]^+$ , 100%), 528 ( $[M^+]$ , 16%).  $^1H$  NMR (400 MHz, DMSO- $d_6$ ):  $\delta$  = 7.95 (t, 1H), 7.48 (d, 3H), 7.46 (s, 1H), 7.43 (d, 2H), 5.50 (s, 4H), 3.92 (s, 6H). Anal. calc. for  $C_{23}H_{23}N_5Br_2$ : C, 52.19; H, 4.38; N, 13.28. Found: C, 51.91; H, 4.44; N, 12.98.

**$L_3$ .** Off-white solid powder, yield: 7.18 g, 86.3%. LC MS-ESI<sup>+</sup>,  $m/z$ : 432 ( $[M^+-Br]^+$ , 100%).  $^1H$  NMR (400 MHz, DMSO- $d_6$ ):  $\delta$  = 9.39 (s, 2H), 8.00 (t, 1H), 7.88 (s, 2H), 7.78 (s, 2H), 7.50 (d, 2H), 5.58 (s, 4H), 4.27 (t, 4H), 1.81 (t, 4H), 1.29 (t, 4H), 0.92 (t, 6H). Anal. calc. for  $C_{21}H_{31}N_5Br_2$ : C, 49.14; H, 6.09; N, 13.64. Found: C, 48.84; H, 5.96; N, 13.40.

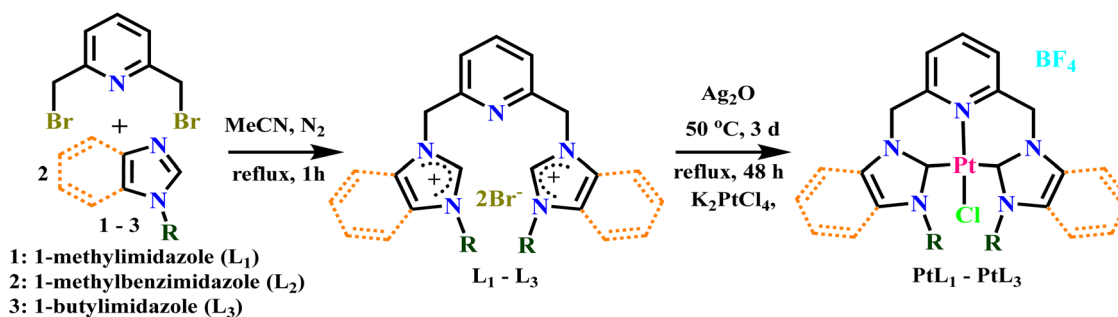
### Synthesis of Pt(II) C<sup>N</sup>C pincer complexes, $PtL_1$ – $PtL_3$

The complexes, 2,6-bis[(3-methylimidazolium-1-yl)methyl]pyridine-(chloro)platinum(II) tetrafluoroborate ( $PtL_1$ ), 2,6-bis[(3-methylbenzimidazol-1-yl)methyl]pyridine-(chloro)platinum(II) tetrafluoroborate ( $PtL_2$ ) and 2,6-bis[(3-butylimidazol-1-yl)methyl]pyridine-(chloro)platinum(II) tetrafluoroborate ( $PtL_3$ ) were synthesized using silver carbene transmetalation method used for similar square planar complexes with minor modifications. The ligand precursor  $L_1$  (1.07 g, 2.5 mmol)/ $L_2$  (1.32 g, 2.5 mmol)/ $L_3$  (1.28 g, 2.5 mmol) was suspended in 50 mL of  $CH_2Cl_2$  and 6 mL of methanol (enhance the dissolution). This was then mixed with  $Ag_2O$  (590.9 mg, 2.55 mmol), resulting in a black suspension that was protected from light and stirred at 50–60 °C for 3 days under a nitrogen atmosphere. The black residue was filtered and washed with methanol. The residue was suspended in 70 mL of  $CH_3CN$ , and then  $AgBF_4$  (496.4 mg, 2.55 mmol) was added, followed by an aqueous solution (5 mL) of  $K_2PtCl_4$  (1.02 g, 2.45 mmol). The resulting mixture was stirred for 48 hours in the darkness under nitrogen. The precipitate was filtered and the orange/yellow residue was washed with  $CH_2Cl_2$  and  $Et_2O$  to yield an orange/yellow solid, which was further dried under vacuum to remove the solvents.  $^1H$  NMR spectra, ESI<sup>+</sup> TOF MS and elemental analysis results are given below; spectra are given in ESI,<sup>†</sup> Fig. S7–S9 and S10–S12, respectively. Scheme 2 shows the schematic procedure for the synthesis of CNC pincer ( $L_1$ – $L_3$ ) and corresponding Pt(II) complexes ( $PtL_1$ – $PtL_3$ ).

**( $L_1PtCl$ ) $BF_4$ ,  $PtL_1$ .** Yield: 1.45 g, 65.8%. TOF-(ESI<sup>+</sup>)-MS,  $m/z$ : 498.03 ( $[M^+-BF_4]$ , 100%).  $^1H$  NMR (400 MHz, DMSO- $d_6$ ):  $\delta$  = 8.29 (t, 1H<sub>Py</sub>), 7.90 (d, 2H<sub>Py</sub>), 7.60 (d, 2H<sub>Im</sub>), 7.40 (d, 2H<sub>Im</sub>), 7.12 (d, 2H<sub>Methine</sub>), 5.46 (m, 4H<sub>Methylene</sub>), 3.92 (s, 6H<sub>Methyl</sub>). Anal. calcd for  $C_{15}H_{19}N_5F_4BClPt$ : C, 30.71, H: 3.26, N: 11.94. Found; C: 30.38, H: 3.11, N: 12.19.

**( $L_2PtCl$ ) $BF_4$ ,  $PtL_2$ .** Yield: 1.28 g, 52.1%. TOF-(ESI<sup>+</sup>)-MS,  $m/z$ : 599.15 ( $[M^+-BF_4]$ , 100%).  $^1H$  NMR (400 MHz, DMSO- $d_6$ ):  $\delta$  = 8.39 (t, 1H<sub>Py</sub>), 8.28 (d, 2H<sub>Py</sub>), 8.04 (m, 4H<sub>BzIm</sub>), 7.84 (d, 2H<sub>Methine</sub>), 7.54 (m, 4H<sub>BzIm</sub>), 6.13 (d, 2H<sub>Methylene</sub>), 5.71 (d, 2H<sub>Methylene</sub>), 4.28 (s, 6H<sub>Methyl</sub>). Anal. cal. for  $C_{23}H_{23}N_5F_4BClPt$ : C, 40.22, H: 3.38, N: 10.20. Found; C: 39.91, H: 3.52, N: 10.09.

**( $L_3PtCl$ ) $BF_4$ ,  $PtL_3$ .** Yield: 1.45 mg, 61.1%. TOF-(ESI<sup>+</sup>)-MS,  $m/z$ : 583.19 ( $[M^+-BF_4]$ , 100%).  $^1H$  NMR (400 MHz, DMSO- $d_6$ ):  $\delta$  = 9.51 (d, 2H<sub>Py</sub>), 8.24 (t, 1H<sub>Py</sub>), 8.09 (d, 2H<sub>Methine</sub>), 6.17 (d, 2H<sub>Im</sub>), 5.66 (d, 2H<sub>Im</sub>), 5.57 (s, 4H<sub>Methylene</sub>), 4.59 (d, 4H<sub>Methylene butyl</sub>), 2.15 (m, 4H<sub>Methylene butyl</sub>), 1.91 (t, 4H<sub>Methylene butyl</sub>), 1.09



Scheme 2 Synthesis of N-heterocyclic carbene ligands  $L_1$ – $L_3$  and their corresponding  $PtL_1$ – $PtL_3$ .

(S, 6H<sub>Methyl N-butyl</sub>). Anal. calcd for C<sub>21</sub>H<sub>31</sub>N<sub>5</sub>F<sub>4</sub>ClPt; C: 37.60, H: 4.66, N: 10.44. Found; C: 37.27, H: 4.49, N: 10.77.

### Stability of the Pt(II) C<sup>N</sup>C pincer complexes PtL<sub>1</sub>–PtL<sub>3</sub> in DMSO/water

The studied complexes PtL<sub>1</sub>–PtL<sub>3</sub> were moderately soluble in water and alcohols. Thus, they were dissolved at requisite quantities in minimum amounts of DMSO (*ca.* 2.0% of final volume) to enhance the solubility and then diluted with aqueous Tris–HCl/50 mM NaCl (pH = 7.2) buffer to a final Pt(II) C<sup>N</sup>C pincer complex concentration of  $5.0 \times 10^{-5}$  M. Thereafter, their solution chemistry/stability under physiological-like conditions was evaluated by studying their rate of chloro substitution with biogenic nucleophiles as well as evaluating their interactions with relevant biological targets using UV-visible absorption and fluorescence emission spectroscopies.

The diluted solutions were analyzed immediately, and the spectra were recorded at 1 hour intervals over 24 hours at 25 °C. The electronic absorption spectra of all three PtL<sub>1</sub>–PtL<sub>3</sub> remained unchanged for 24 hours after dissolution, indicating their good stability (for spectral changes, refer to Fig. S13a–c, ESI<sup>†</sup> for PtL<sub>1</sub>–PtL<sub>3</sub>, respectively).

### Preparation of complexes PtL<sub>1</sub>–PtL<sub>3</sub> and nucleophile solutions

Each Pt(II) C<sup>N</sup>C pincer complex (PtL<sub>1</sub>–PtL<sub>3</sub>) was dissolved at requisite quantities in minimum amounts of DMSO (about 2.0% of final volume) to enhance solubility in 5.0 mM tris(hydroxymethyl)aminomethane, Tris–HCl/50 mM NaCl buffer (pH = 7.2), aqueous medium and NaCl was added to suppress the spontaneous hydrolysis of the complex. The nucleophiles (tu, dmtu and tmtu) were prepared at concentrations 20, 40, 60, 80, 100 and 120 times higher than that of the complexes. This was to ensure that pseudo conditions were maintained at all times.<sup>17</sup> The rates of reactions were measured as a function of concentration and temperature (within 25 to 55 °C at 10 °C intervals).

### Kinetic measurements

Under pseudo-first-order conditions, the rate of chloride substitution from PtL<sub>1</sub>–PtL<sub>3</sub> by thiourea nucleophiles was monitored using a conventional UV-vis spectrophotometer, measuring changes in absorbance at a suitable wavelength as a function of [Nu] and temperature. At all concentrations and temperatures for all the reactions, the kinetic traces were fitted to the first-order exponential function to generate the observed pseudo-first-order rate constants,  $k_{\text{obs}}$ , using the OriginPro 9.1<sup>®</sup> graphical analysis software<sup>18</sup> according to eqn (1):

$$A_t = A_0 + (A_\infty - A_0)e^{(-k_{\text{obs}})t} \quad (1)$$

where  $A_0$ ,  $A_t$  and  $A_\infty$  represent the absorbance of the reaction mixture initially, at time  $t$  and at the end of the reaction respectively. The obtained  $k_{\text{obs}}$  values were plotted against the respective concentration of the nucleophiles.

The temperature dependence of rate data was investigated at 25 to 55 °C with intervals of 10 °C. The activation parameters ( $\Delta H^\ddagger$ ,  $\Delta S^\ddagger$  and  $\Delta G^\ddagger$ ) were computed using the Eyring formula (eqn (2)):

$$\ln(k_2/T) = -\Delta H^\ddagger/RT + (23.8 + \Delta S^\ddagger/R) \quad (2)$$

### Computational calculations

The molecular structures of PtL<sub>1</sub>–PtL<sub>3</sub> were computed using the Gaussian 09 program package.<sup>19</sup> The geometry optimizations, frequency calculations, and molecular orbital mappings were performed using density functional theory (DFT) by the B3LYP functional method utilizing the Los Alamos National Laboratory 2 Double-Zeta (LANL2DZ) basis sets to get reliable results for the late transition metal atoms.<sup>20</sup> The complexes were modeled as monocations of singlet spin state. This was due to the low electronic spin of PtL<sub>1</sub>–PtL<sub>3</sub>. The structural data of the complexes were computed in a water solution, considering solvolysis effects by employing the conductor polarizable model.

### Voltammetric measurements

Electrochemical measurements of PtL<sub>1</sub>–PtL<sub>3</sub> were conducted using an Autolab PGSTAT 302 potentiostat (Eco Chemie, Utrecht, The Netherlands). The instrument has a three-electrode voltammetric cell system comprising a glassy carbon working electrode (GCWE of 1.5 mm radius), a Ag/AgCl (3 M KCl,  $0.015 \pm 0.003$ ) wire as the pseudo reference electrode and a Pt rod as the counter electrode as well as an electrochemical impedance spectroscopy (EIS) module. The Autolab NOVA 1.7 software package was used for controlling the potentiostat and data analysis. In all EIS measurements, 1.0 mM DMSO/tetrabutylammonium hexafluoro-phosphate (0.1 M) solutions of PtL<sub>1</sub>–PtL<sub>3</sub> were used to record the spectral changes at  $25.0 \pm 1.0$  °C. Between each measurement, the GCWE electrode surface was polished with an alumina slurry on a Buehler felt pad, rinsed with excess ultrapure water and ultra-sonicated in absolute ethanol. Cyclic voltammograms/scans were recorded in a potential window of  $-2.0$  to  $+2.0$  V vs. Ag/AgCl. CV scans of PtL<sub>1</sub>–PtL<sub>3</sub> were recorded at different potential scan rates ( $25$ – $250$  mV s<sup>−1</sup>). Further, spectroelectrochemical CV scans (at a scan rate of  $100$  mV s<sup>−1</sup>) accompanying the titration of  $1.0$  mM PtL<sub>1</sub>–PtL<sub>3</sub> with calf-thymus deoxyribonucleic acid (CT-DNA) ( $0.0$  to  $75$  μM) were recorded at each addition to confirm and evaluate the mode of interactions between the two. The data were used to calculate the electrochemical-derived binding constants for the complexes according to eqn (3):

$$\log(1_a/[CT-DNA]) = \log K + \log(I/(I_{a0} - I_a)) \quad (3)$$

where  $K$  is the binding constant, and  $I_{a0}$  and  $I_a$  are the anodic peak currents of the Pt(II) C<sup>N</sup>C pincer complex in the absence and presence of CT-DNA, respectively.

### Viscosity measurements

An Ubbelohde viscometer immersed in a thermostatic water bath kept at  $25 (\pm 0.1)$  °C was used to measure the viscosity. CT-DNA samples were prepared by sonication to minimize the complexity arising from DNA flexibility. Different amounts of each complex were added to CT-DNA at a constant concentration of  $5.0$  mM. After equilibrium for  $15$  min, the flow time of samples was measured in triplicate to obtain the concurrent values using a digital stopwatch. The relative viscosities for CT-DNA in the presence and absence of Pt(II)-NHC complexes or EtBr were calculated using eqn (4):

$$\eta = (t - t_0)/t_0, \quad (4)$$





where  $t$  is the observed flow time of CT-DNA containing the Pt(II) C<sup>N</sup>C pincer complex or EtBr and  $t_0$  is the flow time of the Tris-HCl buffer alone. The viscosity of the solution was presented as a binding ratio,  $(\eta/\eta_0)^{1/3}$ , where  $\eta$  is the viscosity of CT-DNA in the presence of studied Pt(II) C<sup>N</sup>C pincer complex/ EtBr and  $\eta_0$  is the viscosity of CT-DNA alone.

### Binding studies

**Absorption spectral studies with CT-DNA.** PtL<sub>1</sub>-PtL<sub>3</sub>/CT-DNA titrations to evaluate the strength of the binding interactions were performed at room temperature (25 °C) in 5 mM tris(hydroxymethyl)aminomethane and Tris-HCl/50 mM NaCl buffer (pH = 7.2, stored at 4 °C in the darkness and used within 4 days). A 5.0 mM stock solution of PtL<sub>1</sub>-PtL<sub>3</sub> was prepared in 2.0% DMSO. It has been verified that low-concentration DMSO solutions of the complexes or DNA solution do not interfere with the kinetic integrity of the complexes nor the conformation stability of DNA. The concentration of CT-DNA was pre-determined from a Beer-Lambert plot by measuring the absorption intensity at 260 nm, where the molar absorptivity of CT-DNA is about 6600 M<sup>-1</sup> cm<sup>-1</sup>. The absorbance ratio at 260 and 280 nm ( $A_{260}/A_{280}$ ) was determined to be in the range of 1.8 to 1.9, indicating that the DNA was sufficiently free of protein.<sup>21</sup>

A 20.0 μM of PtL<sub>1</sub>-PtL<sub>3</sub> solution was titrated spectrophotometrically with the increasing CT-DNA concentration (0–20 μM). To eliminate the absorbance of CT-DNA, requisite amounts of CT-DNA were added to both the reference and the sample (PtL<sub>1</sub>-PtL<sub>3</sub>/CT-DNA) cuvettes and both samples were allowed to incubate for 10 minutes before recording the background corrected absorption spectrum of PtL<sub>1</sub>-PtL<sub>3</sub>. The absorption changes of the MLCT bands of the complexes were monitored as [CT-DNA] was increased. The binding constants of the Pt(II) C<sup>N</sup>C pincer complexes were calculated using the Wolfe-Shimer equation presented as eqn (5):<sup>22</sup>

$$[\text{CT-DNA}]/(\epsilon_a - \epsilon_f) = [\text{CT-DNA}]/(\epsilon_b - \epsilon_f) + 1/(K_b(\epsilon_b - \epsilon_f)) \quad (5)$$

where [CT-DNA] is the concentration of CT-DNA, and  $\epsilon_a$ ,  $\epsilon_f$  and  $\epsilon_b$  are the molar absorptivities of the titrated mixture ( $A_{\text{obs}}/[\text{complex}]$ ), unbound Pt(II) C<sup>N</sup>C pincer complex and the Pt(II) C<sup>N</sup>C pincer/CT-DNA complex, respectively.  $K_b$  is the binding constant calculated from the ratio of the slope to intercept for the plot of  $[\text{CT-DNA}]/(\epsilon_a - \epsilon_f)$  versus [CT-DNA]. The standard Gibbs free energy ( $\Delta G$ ) of the Pt(II) C<sup>N</sup>C pincer complexes bound to CT-DNA was obtained using the van't Hoff equation presented as eqn (6):

$$\Delta G = -RT \ln K_b \quad (6)$$

**Absorption spectral studies of PtL<sub>1</sub>-PtL<sub>3</sub> with bovine serum albumin (BSA).** To probe the strength of the interactions between PtL<sub>1</sub>-PtL<sub>3</sub> and bovine serum albumin (BSA), aliquots of a fixed concentration of BSA (10 μM) were titrated with a fixed concentration (5 μM) of each complex (PtL<sub>1</sub>-PtL<sub>3</sub>) and the accompanying changes recorded spectrophotometrically. Moreover, the UV-vis absorption spectra help understand the type of

quenching (either static nor dynamic) between PtL<sub>1</sub>-PtL<sub>3</sub> and BSA. The enhancement with a prominent blue shift and the diminishing with a prominent red shift in the absorption intensity of BSA with the addition of each complex with reference to the BSA absorption intensity signify that the quencher (metal complexes) quenches the fluorescence intensities of BSA in static and dynamic manners, respectively. Static quenching refers to the formation of fluorophore and quencher complex adduct in the ground state, whereas in dynamic quenching the fluorophore and the quencher get in touch with each other during the transient existence of the excited state.<sup>23</sup>

**Fluorescence spectral studies with CT-DNA.** DNA preloaded with 3,8-diamino-5-ethyl-6-phenylphenanthridinium bromide (EtBr) is highly emissive such that its quenching by metal complexes can be used to probe their interactions with it. EtBr is a planar cationic dye that inserts between adjacent CT-DNA base pairs through its planar phenanthridine ring to form soluble and highly fluorescent complexes with nucleic acids. The formation of an EtBr + CT-DNA adduct *via* intercalation is readily detected in the emission spectrum of EtBr upon the addition of CT-DNA, as an intense fluorescence emission at 596 nm, when excited at 510 nm owing to the extraneous rigidity of its immediate environment in the solution phase.<sup>24</sup> Thus, the competitive DNA binding studies were carried out using PtL<sub>1</sub>-PtL<sub>3</sub> by following the quenching of the fluorescence emission intensity of the EtBr-DNA complex after each addition of the Pt(II) complexes. The DNA fluorescence quenching titrations with PtL<sub>1</sub>-PtL<sub>3</sub> were performed using DNA preloaded EtBr. A fixed concentration of CT-DNA-EtBr (10.0 μM each of CT-DNA and EtBr) was prepared in a 5 mM Tris-HCl/50 mM NaCl buffer (pH = 7.2). This solution was stored at 4 °C for 4 hours. The competitive binding effects of the complexes PtL<sub>1</sub>-PtL<sub>3</sub> on the CT-DNA-EtBr complex were monitored by adding variable aliquots of 5.0 mM PtL<sub>1</sub>-PtL<sub>3</sub> to the 10.0 μM CT-DNA + EtBr solutions. The decrease in the DNA/EtBr emission was recorded within the wavelength range of 520–700 nm after excitation of the solutions at 500 nm. Before recording the spectra, the overlays of the formed DNA/PtL<sub>1</sub>-PtL<sub>3</sub> adducts were thermally pre-equilibrated, mixed thoroughly, and incubated for 10 minutes. The quenching efficiency of the complexes was analyzed using the Stern-Volmer formula (eqn (7)).<sup>25</sup>

$$I_0/I = 1 + K_{sv}[Q] = 1 + k_q\tau_0[Q] \quad (7)$$

where  $I_0$  and  $I$  are the emission intensities of the CT-DNA + EtBr complex in the absence and each addition of a complex, respectively and  $[Q]$  is the concentration of PtL<sub>1</sub>-PtL<sub>3</sub> (the quenchers,  $Q$ ). The Stern-Volmer (quenching) constant  $K_{sv}$  was determined from the slope of the linear plot of  $I_0/I$  versus  $[Q]$ . To gain an insight into the kinetics of the competitive binding process, the bimolecular quenching rate constant ( $k_q$ ) values were also computed using eqn (8):

$$K_{sv} = k_q\tau_0 \quad (8)$$

where  $\tau_0$  is the average fluorescence lifetime of the CT-DNA/EtBr complex in the absence of the quencher and its value is 23



nanoseconds at room temperature.<sup>26</sup> The apparent binding constant,  $K_{\text{app}}$  was computed using eqn (9):

$$K_{\text{EtBr}}[\text{EtBr}] = K_{\text{app}}[\text{Q}] \quad (9)$$

where  $[\text{Q}]$  is the concentration of the quencher causing a 50% reduction in the fluorescence intensity of the CT-DNA/EtBr adduct,  $K_{\text{EtBr}}^{27} = 1.0 \times 10^7 \text{ M}^{-1}$  and  $[\text{EtBr}]$  was taken as 60, 30 and 25  $\mu\text{M}$  for **PtL<sub>1</sub>–PtL<sub>3</sub>**, respectively. Scatchard plots also gave the binding constant  $K_F$  as determined from the fluorescence titration using the Scatchard formula (eqn (10)):<sup>28</sup>

$$\log(I_0 - I)/I = \log K_F + n \log[\text{Q}] \quad (10)$$

where  $n$  is the number of binding sites per nucleotide.

**Fluorescence spectral studies with BSA.** Fluorescence quenching titrations of BSA with **PtL<sub>1</sub>–PtL<sub>3</sub>** were performed to determine their binding constants on the protein residues of BSA. The concentration of BSA was measured spectrophotometrically using the Beer–Lambert formulation where an  $\epsilon_{\text{max}}$  value of  $4.4 \times 10^4 \text{ M}^{-1} \text{ cm}^{-1}$  was assumed at 278 nm ( $\lambda_{\text{max}}$ ).<sup>29</sup> The stock concentration of BSA (10.4  $\mu\text{M}$ ) was prepared in 5 mM Tris–HCl/50 mM NaCl buffer at pH = 7.2. The overlay emission spectra of the pre-equilibrated 30  $\mu\text{M}$  of buffered BSA solutions in the absence and presence of **PtL<sub>1</sub>–PtL<sub>3</sub>** (of concentration ranging from 0 to 130  $\mu\text{M}$ ) were recorded at room temperature. The emission changes were recorded in the  $\lambda_{\text{em}}$  range of 250 to 450 nm, with the excitation wavelength set at 278 nm after a pre-incubation time of 10 minutes. The quenching efficiency of **PtL<sub>1</sub>–PtL<sub>3</sub>** was calculated using the Stern–Volmer formula (eqn (7)) as discussed above. The Stern–Volmer (quenching) constant  $K_{\text{sv}}$  was determined from the slope of the linear plot of  $I_0/I$  versus  $[\text{Q}]$ . To gain an insight into the kinetics of the competitive binding process, the bimolecular quenching rate constant ( $k_q$ ) values were also computed using eqn (8), where  $\tau_0$  is the average fluorescence lifetime of the BSA alone (ca. 10 nanoseconds).<sup>30</sup> Scatchard plots also gave the binding constant  $K_F$  as determined from the fluorescence titration data using eqn (10).

**Filter effect absorbance corrections.** The filter effect also termed the inner filter effect (IFE) is an inherent spectral interference, whereby the emission band overlaps with the absorption bands of solution constituents, including the fluorophore causing self- or overlap-absorption of fluorescence emission.<sup>31</sup> To evaluate the primary and/or secondary IFE, a Shimadzu UV-1800 UV-visible spectrophotometer was used. The fluorescence intensities were measured at excitation and emission wavelengths of 510/280 and 597/347 nm for CT-DNA or BSA, respectively. To eliminate the probability of re-absorption and the IFE of **PtL<sub>1</sub>–PtL<sub>3</sub>**, the fluorescence data of CT-DNA/BSA were corrected for absorption of excitation and emitted light correction factor according to eqn (11):<sup>32</sup>

$$F_{\text{corr}} = F_{\text{obs}} 10^{(A_{\text{ex}} + A_{\text{em}})/2} \quad (11)$$

where  $F_{\text{corr}}$  and  $F_{\text{obs}}$  are the corrected and observed fluorescence intensities, respectively, caused by quencher/fluorophore addition in a 1 cm path-length cuvette. The correction factor is valid and applicable in the case of typical fluorophores where scattering is negligible and the extinction is dominated by absorption.

**In silico docking simulations.** To study the binding mode and intermolecular interactions of **PtL<sub>1</sub>–PtL<sub>3</sub>** with DNA/BSA, docking studies using the online server programs PatchDock and FireDock were performed. In the simulations, **PtL<sub>1</sub>–PtL<sub>3</sub>** and DNA or BSA were used as the guest and host/receptor molecules, respectively. High-quality three-dimensional (3D) structures of **PtL<sub>1</sub>–PtL<sub>3</sub>** in the PDB format were obtained by converting CHK files of the DFT-optimised structures using the Gaussian 09W software. The 3D-crystallized structure of the target receptor of duplex DNA (PDB ID: 1F8N of the base sequence: (ACCGACGTCGGT)<sub>2</sub>) or BSA (PDB ID: 3VO3) was taken from the Protein Data Bank (<https://www.rcsb.org/pdb>) at resolutions of 1.60 and 2.47 Å, and  $r$ -values of 0.206 and 0.259 were obtained for DNA and BSA, respectively. DNA receptor molecules were prepared by amending the crystal structures of B-DNA, whereby water molecules of crystallization were omitted, while the BSA structure was further altered by eliminating the calcium ions and the second co-crystallized BSA molecule. Afterward, the preliminary structures of B-DNA or BSA were edited by adding all hydrogens followed by the merging of non-polar hydrogens and computations of the Gasteiger charges. A binding site was chosen on the BSA or DNA that could snugly fit the guest molecules but allow them to rotate freely. Docked conformations of the energy, obtained by simulating and optimizing the binding modes of the host with **PtL<sub>1</sub>–PtL<sub>3</sub>**, were calculated. The simulated docked poses were refined using FireDock. Out of 10 different conformers, the lowest binding energy conformer was selected for analysis. Docked poses and their perspective views were visualized using the CHIMERA (<https://www.cgl.ucsf.edu/chimera>) molecular graphics program.

## Results and discussion

### Substitution kinetics

The rate of substitution of chloride from **PtL<sub>1</sub>–PtL<sub>3</sub>** by S-donor nucleophiles (tu, dmtu and tmtu) was followed by using a conventional UV-vis spectrophotometer, measuring the changes in absorbance at a suitable wavelength as a function of  $[\text{Nu}]$  and time. Typical spectral changes due to the reaction of the complex **PtL<sub>1</sub>** with tu are shown in Fig. 1. The inset shows a typical kinetic trace of absorbance versus time at  $\lambda = 286 \text{ nm}$  and  $T = 35^\circ\text{C}$ , which was fitted to the first-order exponential function to generate the observed pseudo-first-order rate constants,  $k_{\text{obs}}$ , in the OriginPro 9.1<sup>®</sup> graphical analysis software according to eqn (1). The linear dependence of  $k_{\text{obs}}$  versus  $[\text{Nu}]$  was observed for all reactions with positive intercepts, as shown in Fig. 2, for plots at  $35^\circ\text{C}$ . For data at other temperatures, refer to Fig. S14 and S15 (ESI<sup>†</sup>). The second-order rate constants  $k_2$  for the reactions of **PtL<sub>1</sub>–PtL<sub>3</sub>** with the Nus were obtained from the slopes of the linear plots of  $k_{\text{obs}}$  versus  $[\text{Nu}]$ , according to the rate equation  $k_{\text{obs}} = k_2[\text{Nu}] + k_s$ , where  $k_s$  is the first-order rate constant for the solvent path associated with the reactions. The rate law further indicates that the entering thiourea nucleophiles (tu, dmtu and tmtu) irreversibly displaced the chloride co-ligand from the mono-functional Pt(II) metal complexes (**PtL<sub>1</sub>–PtL<sub>3</sub>**), as supported



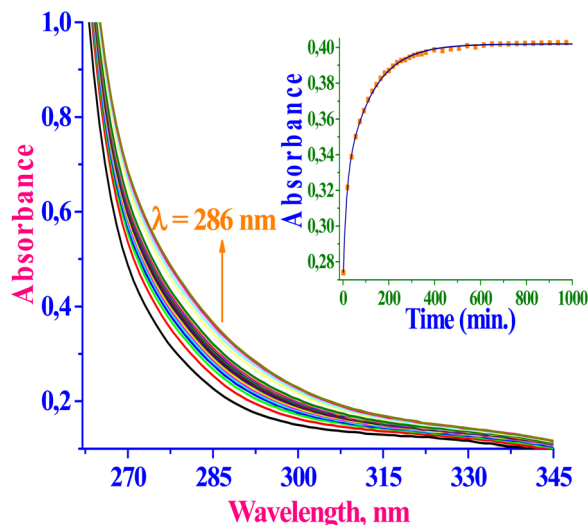


Fig. 1 UV-vis spectral changes for the reaction between **PtL<sub>1</sub>** (50  $\mu$ M) and Tu (40-fold excess). Inset: Typical kinetic trace of absorbance versus time at  $\lambda = 286$  nm, 5 mM Tris-HCl/50 mM NaCl (pH = 7.2) and  $T = 35$   $^{\circ}$ C.

by the ligand exchange reaction kinetic traces of reactions of similarly structured Pt/Pd(II) complexes found in the literature.<sup>33–36</sup> The rate data at 35  $^{\circ}$ C are summarized in Table 1, and data at other temperatures are given in Table S1 (ESI<sup>†</sup>).

### Temperature effect and iso-kinetic relationship

The temperature dependence of  $k_2$  was investigated within the temperature range of 25 to 55  $^{\circ}$ C at intervals of 10  $^{\circ}$ C. The activation parameters were computed using the Eyring formula (eqn (2)), and the values are presented in Table 1, while the plots are given in Fig. S16 (ESI<sup>†</sup>). The large negative entropy of activation ( $\Delta S^{\ddagger}$ ) and low but positive enthalpy of activation ( $\Delta H^{\ddagger}$ ) indicate an associative mechanism that signifies the formation of energetically favourable new bonds between **PtL<sub>1</sub>**–**PtL<sub>3</sub>** and incoming nucleophiles in the transition state. Moreover, the comparable  $\Delta G_{35^{\circ}\text{C}}^{\ddagger}$

values suggest that these reactions essentially follow the same mechanism.<sup>37,38</sup> Iso-kinetic linear plots of  $\Delta H^{\ddagger}$  versus  $\Delta S^{\ddagger}$  (ESI<sup>†</sup>, Fig. S17) from a linear free energy relationship (LFER) between the activation parameters further signify that all the reactions follow a similar associatively activated mechanism<sup>39,40</sup> From the plot, the iso-kinetic temperatures and  $\Delta G^{\ddagger}$  for the chloride substitution from **PtL<sub>1</sub>**–**PtL<sub>3</sub>** were found to be 294 K and 85 kJ mol<sup>–1</sup>, respectively.

As we observed and stated *vide supra*, the kinetic traces fit into a first-order exponential function, indicating that the substitution is first order and takes place in a single step, *i.e.*, the substitution of chloride by incoming Nus, and there is no further reaction (*i.e.*, no dechelation of the C<sup>N</sup>C pincer ligand from **PtL<sub>1</sub>**–**PtL<sub>3</sub>**). This is probably owing to the strong  $\sigma$ -donor and weak  $\pi$ -acceptor property of the C<sup>N</sup>C pincer ligand.<sup>41</sup> Moreover, the high basicity of the C<sup>N</sup>Cs prompts the formation of stronger (dative  $\sigma$ -) bonds with the Pt(II) ions. The Pt–C/N bond length falls in the range of typical Pt–N/C single bond lengths.<sup>42</sup> The bis(NHC) ligands are electronically and sterically adjustable, which further stabilizes their complexes.<sup>43</sup> Thus, breaking the bond (dechelation) between Pt(II) and the C<sup>N</sup>C pincer ligand is energetically unfavourable. This is further reinforced by the large  $-\Delta S^{\ddagger}$  and positive  $\Delta H^{\ddagger}$  values (*vide supra* Table 1) for the associatively activated mechanism for the chloride substitution by thiourea nucleophiles.<sup>44,45</sup>

The elucidation of the role of the C<sup>N</sup>C pincer ligands on the rate was fostered by extending phenyl pendant rings and *N*-butyl arms, respectively on the *cis* position to the leaving group of the core C<sup>N</sup>C pincer ligand of **PtL<sub>2</sub>** and **PtL<sub>3</sub>** relative to the structure of **PtL<sub>1</sub>**. Comparing the rate constant values for the chloride substitution from the complexes (**PtL<sub>1</sub>**–**PtL<sub>3</sub>**) with S-donor thiourea Nus (Table 1), all complexes follow the reactivity order **PtL<sub>3</sub>** < **PtL<sub>2</sub>** < **PtL<sub>1</sub>**. Lower reactivity for the complex **PtL<sub>2</sub>** than that of **PtL<sub>1</sub>** is probably owing to the enhanced  $\sigma$ -inductive effect by extended  $\pi$ -conjugation *via cis*-carbon atoms, which further stabilizes the Pt(II) metal centre, thereby retarding the rate of chloride substitution. While the

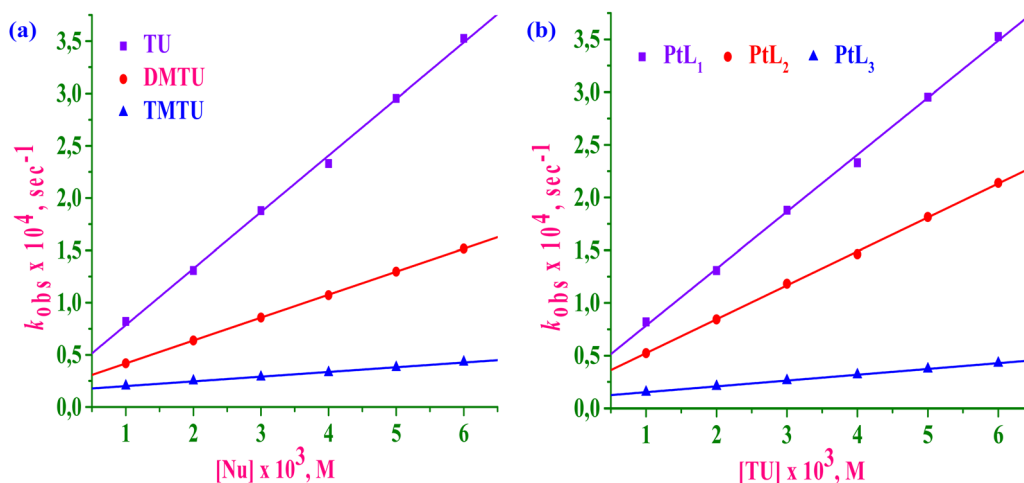
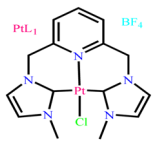
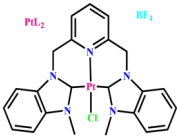



Fig. 2 Linear plots of  $k_{\text{obs}}$  versus  $[\text{Nu}]$  for the reaction of **PtL<sub>1</sub>** with Nus (a) and for the reactions with three Pt(II) C<sup>N</sup>C pincer complexes (**PtL<sub>1</sub>**, **PtL<sub>2</sub>** and **PtL<sub>3</sub>**) with Tu (b):  $[\text{PtL}_1/\text{PtL}_2/\text{PtL}_3] = 50$   $\mu$ M, pH = 7.2 (5 mM Tris-HCl/50 mM NaCl) and  $T = 35$   $^{\circ}$ C.



**Table 1** Summary of the second-order rate constants  $k_2$  at 35 °C and activation parameter values for the substitution of chloride molecules by Tu nucleophiles

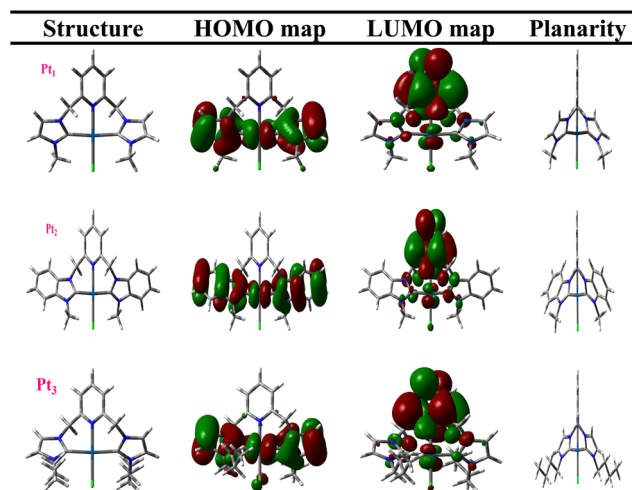
Complex	Nu	$k_2 \times 10^2/\text{M}^{-1} \text{s}^{-1}$	$\Delta H^\ddagger/\text{kJ mol}^{-1}$	$-\Delta S^\ddagger/\text{J mol}^{-1} \text{K}^{-1}$	$\Delta G_{35^\circ\text{C}}^\ddagger/\text{kJ mol}^{-1}$
 PtL <sub>1</sub>	tu	5.41 ± 0.20	57 ± 3	84 ± 2	83 ± 1
	dmtu	2.20 ± 0.13	80 ± 5	18 ± 1	85 ± 2
	tmtu	0.45 ± 0.07	38 ± 2	167 ± 8	90 ± 2
 PtL <sub>2</sub>	tu	3.21 ± 0.17	68 ± 4	55 ± 2	84 ± 1
	dmtu	1.48 ± 0.11	82 ± 5	15 ± 1	88 ± 2
	tmtu	0.37 ± 0.05	41 ± 2	159 ± 7	90 ± 3
 PtL <sub>3</sub>	tu	0.55 ± 0.07	37 ± 2	169 ± 8	89 ± 2
	dmtu	0.21 ± 0.03	55 ± 3	119 ± 3	91 ± 3
	tmtu	0.07 ± 0.01	54 ± 3	130 ± 3	94 ± 3

least reactivity for **PtL<sub>3</sub>** is most likely attributed to the steric hindrance caused by its free *N*-butyl arms, which limits the space around the metal centre and eventually lowers its reactivity, a detailed discussion is given *vide infra*. The data presented in Table 1 further show that the substitution of chloride decreases with the increasing bulk of the incoming nucleophile and the increasing reactivity order follows tmtu < dmtu < tu. Relatively, tmtu is the bulkiest and offers the most steric hindrance towards the nucleophilic attack of the complexes, and this results in its least reactivity with the Pt(II) C<sup>N</sup>^C pincer complexes compared to the other two nucleophiles.<sup>46</sup>

## Computational analysis

Density functional theory (DFT) theoretical calculations were performed to get an in-depth understanding of the structural as well as electronic differences of the complexes. The DFT-calculated geometry-optimized structures and frontier orbital energy maps for the HOMO and LUMO are presented in Fig. 3, while the geometrical data are summarized in Table S2 (ESI†).

The C<sup>N</sup>^C (bis(3-methylimidazolium-1-yl)pyridine) ligands stabilize the metal centre by  $\sigma$ -donation inductively *via cis*-carbon atoms.<sup>47,48</sup> When a  $\pi$ -conjugation system is attached to the core (*e.g.* addition of phenyl pendant rings), a greater electronic charge dispersion (*i.e.*, a positive  $\sigma$ -inductive effect) occurs. This enhances  $\pi$ -delocalization and  $\sigma$ -inductive effects, which further stabilizes the complex. Thus, the complex **PtL<sub>2</sub>** is stabilized by the extended  $\pi$ -surface of the lateral imidazole rings owing to their enhanced inductive  $\sigma$ -donation *via the cis*-positioned bonds when compared to **PtL<sub>1</sub>**. Consequently, chloride substitution from **PtL<sub>2</sub>** occurs at retarded rates compared to **PtL<sub>1</sub>**.<sup>49</sup> Further, the LUMO orbital energy increased with the increase in the size of the  $\pi$ -surface ( $E_{\text{LUMO}}$  of **PtL<sub>1</sub>** (and  $-2.39$ ) < **PtL<sub>2</sub>** ( $-2.23$  eV)) which indicates an increase in the total

**Fig. 3** DFT-optimized structures, HOMO and LUMO maps for Pt(II) C<sup>N</sup>^C pincer complexes calculated by the B3LYP/LANL2DZ method.

antibonding MO character or an increased localization of the  $\pi^*$  orbitals on the latter ring. This further destabilizes the  $\pi^*$  orbitals of **PtL<sub>2</sub>**, which makes it a poor  $\pi$ -acceptor. Thus, its reactivity is lower than that of **PtL<sub>1</sub>** due to the formation of a more destabilized transition state.<sup>50,51</sup> Further, a direct relationship between the reactivity trend and  $\Delta E_{\text{LUMO-HOMO}}$ , as well as the electrophilicity indices (refer to Table S2, ESI†), is noted to increase with the  $\pi$ -surface of the coordinated imidazolyl rings. On the contrary, Pt NBO charges for **PtL<sub>2</sub>** are raised (+0.261) when compared to **PtL<sub>1</sub>**'s (+0.242), despite the change in the size of the  $\pi$ -surface, suggesting that the Pt atom in the former complex is experiencing lower electron density from the coordinated tridentate ligand. However, the electrophilicity indices should not be confused with the NBO charge, as it denotes the individual atomic charge. The former designates





the overall affinity for negative charge (electrons) based on the electronic properties of the coordinated ligands.<sup>52</sup> Thus, the electrophilicity index is a more suited parameter in predicting the substitutional reactivity of metal complexes than the calculated NBO charges on the individual atoms.<sup>53,54</sup> Thus, the decrease in electrophilicity indices from 4.79 (**PtL<sub>1</sub>**) to 4.46 (**PtL<sub>2</sub>**) implies lower reactivity for the former, which corroborates with the observed reactivity trend between the two.

From Fig. 3, the frontier orbital energy mappings of **PtL<sub>2</sub>** or **PtL<sub>3</sub>** show that both the *N*-substituents (methyl and butyl) did not contribute to either HOMO/LUMO, indicating that the substituents have little to no electronic effect on the frontier orbitals and, hence, the reactivity of both complexes. However, **PtL<sub>3</sub>**, the complex bearing *N*-butyl arms on the imidazole moiety, showed the least reactivity compared to both **PtL<sub>1</sub>** and **PtL<sub>2</sub>**, thus pointing the reactivity difference to steric factors. The *cis*-positioned and longer chain *N*-butyl arms hinder the nucleophilic attack of the Cl ligand more than the methyl groups on **PtL<sub>2</sub>**, thus leading to lower rate constants than those of **PtL<sub>2</sub>** or **PtL<sub>1</sub>**. If one considers the Cl proximal hydrogen distance (Cl...H), it decreases from 2.69 Å (for **PtL<sub>1</sub>**) to 2.05 Å (for **PtL<sub>3</sub>**) indicating that the latter complex has greater steric congestion around the labile ligand, as also illustrated in Fig. S18 (ESI†). This ratifies that the reactivity of the complex, **PtL<sub>3</sub>** is driven by steric rather than electronic factors. Overall, the reactivity of **PtL<sub>2</sub>** and **PtL<sub>3</sub>** when compared with **PtL<sub>1</sub>** is predominantly controlled by the enhanced  $\sigma$ -inductive effect and steric restrictions by the C<sup>N</sup>^C pincer ligands, respectively, and the increasing order is as follows: **PtL<sub>3</sub>** < **PtL<sub>2</sub>** < **PtL<sub>1</sub>**.

### Electrochemical studies

To investigate the electrochemical behaviour of **PtL<sub>1</sub>**–**PtL<sub>3</sub>**, the cyclic voltammetry (CV) technique was employed. Cyclic voltammograms of 1.0 mM **PtL<sub>1</sub>**–**PtL<sub>3</sub>** were recorded in the potential window of –2.0 to +2.0 V, at a scan rate of 250 mV s<sup>–1</sup>, in a phosphate buffer (PBS), pH 7.2, as illustrated in Fig. 4. All

complexes for **PtL<sub>1</sub>**–**PtL<sub>3</sub>** are irreversibly reduced (Pt(II)/Pt(I), as evidenced by a well-defined cathodic peak with no return peak on the anodic scan. The absence of an oxidation wave indicates that the forward cathodic reaction is followed by a fast chemical reaction (*i.e.*, electron transfer followed by a chemical reaction referred to as EC mechanism) that depletes the reduced form (Pt(I)) of the complexes in the solution.<sup>55,56</sup> The reduction peaks ( $E_{pc}$ ) occur at –1.07, –1.21 and –1.34 V for the **PtL<sub>1</sub>**, **PtL<sub>2</sub>** and **PtL<sub>3</sub>**, respectively. It is known that the electron-donating groups on the ligand increase the electron density in the imidazole rings of the coordinated ligands, making reduction more difficult.<sup>57</sup> In other words, the complexes with the poor  $\pi$ -accepting property and more electron-rich ligands have more negative reduction potentials applies  $E_{pc}$  values at higher negative values *i.e.*, Pt(II), leading to lower reactivity. Consequently, **PtL<sub>2</sub>**'s reduction potential appears at a more negative value (–1.21 V) since it bears a bis-NHC chelating ligand with extended  $\pi$ -conjugation when compared with **PtL<sub>1</sub>** (–1.07 V), which lowers the reactivity. Similar results were reported where the reduction peaks shifted to more negative values with each successive addition of phenyl rings owing to molecular distortions of the fused phenyl rings rather than the electronic effect of increasing  $\pi$ -delocalization which provides a greater stabilization to the negative charge.<sup>58,59</sup> Due to the higher electron-donating *N*-butyl groups in the *cis* positions of **PtL<sub>3</sub>**, its  $E_{pc}$  value is less negative (–1.34 V) than that of the complex **PtL<sub>1</sub>** (–1.07 V), showing that its Pt atom is easier to reduce due to its higher electron density. This *cis* effect<sup>49</sup> lowers its reactivity towards incoming nucleophiles, and the details are given in *vide supra*.

Further, the voltammetric responses of 1.0 mM **PtL<sub>1</sub>**–**PtL<sub>3</sub>** were recorded as a function of scan rate at intervals of 25 mV s<sup>–1</sup> (25–250 mV s<sup>–1</sup>) in a phosphate buffer (PBS), pH 7.2. Typical overlays of CVs of 1.0 mM **PtL<sub>1</sub>** at different scan rates are shown in Fig. 5, while those for **PtL<sub>2</sub>** and **PtL<sub>3</sub>** are given

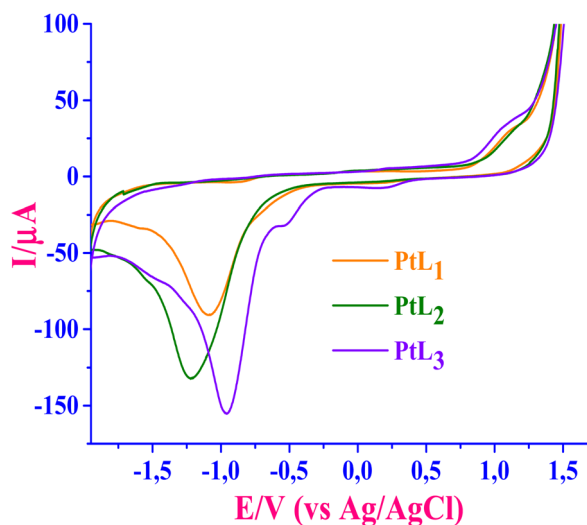


Fig. 4 Cyclic voltammograms of Pt(II) C<sup>N</sup>^C pincer complexes (1.0 mM each) at GCE at a scan rate of 250 mV s<sup>–1</sup>.

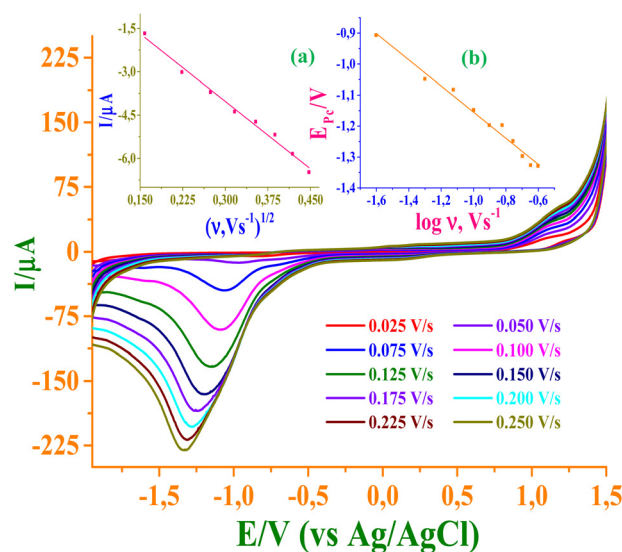


Fig. 5 Effect of the scan rate on the CV for 1.0 mM of **PtL<sub>1</sub>** at different scan rates from 25 to 250 mV s<sup>–1</sup>. Insets (a) and (b): linear relationship between  $I_{pc}$  versus  $(v)^{1/2}$  and  $E_{pc}$  versus  $\log(v)$ , respectively.



in Fig. S19 and S20 (ESI<sup>†</sup>), respectively. Linear dependency of peak intensities  $I_p$  versus scan rate ( $\nu$ ) indicates that electron transfer between the electrode and **PtL**<sub>1</sub>–**PtL**<sub>3</sub> is affected by the rate of reduction of surface-immobilized species.<sup>55</sup> The increase in the cathodic current was accompanied by a shift in cathodic peak potential towards a more negative potential, indicating that all the electrode reactions are irreversible.<sup>60</sup> The plot represents the reduction current peak ( $I_{pc}$ ) versus the square root of scan rate, showing a linear relationship (see inset 'a' of Fig. 5 for **PtL**<sub>1</sub> and inset 'a' of Fig. S19 and S20, ESI<sup>†</sup> for **PtL**<sub>2</sub> and **PtL**<sub>3</sub>, respectively) suggesting that the mass-transport process is most likely diffusion of electroactive species from the electrolyte to the electrode interface, *i.e.*, a typical diffusion-controlled electrode process<sup>61–63</sup> according to the equations:  $I_{pc}$  ( $\mu A$ ) =  $-15.587\nu^{1/2}$  ( $V s^{-1}$ )<sup>1/2</sup> + 0.650;  $R^2 = 0.991$ ,  $I_{pc}$  ( $\mu A$ ) =  $-79.887\nu^{1/2}$  ( $V s^{-1}$ )<sup>1/2</sup> + 20.952;  $R^2 = 0.989$  and  $I_{pc}$  ( $\mu A$ ) =  $-32.381\nu^{1/2}$  ( $V s^{-1}$ )<sup>1/2</sup> + 7.602;  $R^2 = 0.916$  for **PtL**<sub>1</sub>, **PtL**<sub>2</sub> and **PtL**<sub>3</sub>, respectively. However, the fitted curves show non-zero interpenetration related to augmentation by the phase transformation of the GCWE, which led to a deviation from the linearity of these plots.<sup>62</sup> The irreversibility of the reaction process was further confirmed by a linear relationship between the reduction peak potential ( $E_{pc}$ ) and the logarithm of scan rate (see inset 'b' of Fig. 5 for **PtL**<sub>1</sub> and insets 'b' of Fig. S19 and S20 (ESI<sup>†</sup>), for the other two complexes) according to the following equations:

$E_p$  (V) =  $-0.178 \log \nu$  ( $V s^{-1}$ ) – 1.119;  $R^2 = 0.979$ ,  $E_p$  (V) =  $-0.540 \log \nu$  ( $V s^{-1}$ ) – 1.737;  $R^2 = 0.988$  and  $E_p$  (V) =  $-0.422 \log \nu$  ( $V s^{-1}$ ) – 1.579;  $R^2 = 0.996$  for **PtL**<sub>1</sub>, **PtL**<sub>2</sub> and **PtL**<sub>3</sub>, respectively.

### CT-DNA interactions

**UV-Visible absorption studies.** The interactions between **PtL**<sub>1</sub>–**PtL**<sub>3</sub> and CT-DNA were monitored by following the changes in the absorbance upon the addition of CT-DNA (0–40  $\mu M$ ) to a fixed concentration (48  $\mu M$ ) of each **PtL**<sub>1</sub>/**PtL**<sub>2</sub>/**PtL**<sub>3</sub>. The spectral overlays showed a hypochromic shift with the increase in CT-DNA concentration. A typical graph is given in Fig. 6 for the spectral changes due to the **PtL**<sub>1</sub>/CT-DNA interactions, and also see Fig. S21a and b (ESI<sup>†</sup>), for spectral changes of the other **PtL**<sub>2</sub>–**PtL**<sub>3</sub>. The observed decrease in intensity may be due to the stacking of the complexes between nucleic acid base pairs or their groove-binding,<sup>64</sup> both of which alter the helical structure, leading to the observed decrease in the DNA's absorbance intensity. However, no bathochromic shift was observed. This ruled out the intercalative mode of interaction. Thus, **PtL**<sub>1</sub>–**PtL**<sub>3</sub> binds onto CT-DNA strongly most likely by the groove binding mode of interactions. Groove binding is stabilized mainly by hydrogen bonding between complexes and CT-DNA or non-covalent interactions with the edge of the base pairs of the DNA grooves. The magnitude of hypochromism or the shift depends on the strength of the interactions between them as measured by the intrinsic binding constant  $K_b$ . The  $K_b$  values were calculated using eqn (5), and are presented in Table 2. The magnitude of binding constants ( $10^4 M^{-1}$ ) indicates moderate binding strength between the complexes and DNA. The binding constants were used to calculate the Gibbs free energy and  $\Delta G$  values using eqn (6). The values were found to be  $-24.61$ ,  $-23.92$ , and  $-22.60$  kJ mol<sup>−1</sup> for **PtL**<sub>1</sub>, **PtL**<sub>2</sub> and **PtL**<sub>3</sub>, respectively. The negative values of  $\Delta G$  indicate the spontaneity of the binding process of the studied complexes with CT-DNA. The order of magnitude signifies that the complex **PtL**<sub>1</sub> has stronger binding interactions, while **PtL**<sub>3</sub> has the least interactions, and the decreasing order is as follows: **PtL**<sub>1</sub> > **PtL**<sub>2</sub> > **PtL**<sub>3</sub>.

**Fluorescence quenching studies.** Et-Br is a compound that strongly intercalates in between adjacent CT-DNA base pairs through its planar phenanthridine ring. The formation of an EtBr + CT-DNA adduct *via* intercalation is readily detected in the emission spectrum of EtBr upon the addition of CT-DNA, as an intense fluorescence emission at 596 nm, when excited at 510 nm. The monitoring of changes in the fluorescence emission spectra of the EtBr + CT-DNA adduct in the absence and presence of increasing amounts of each Pt(II) C<sup>N</sup>C pincer complex (**PtL**<sub>1</sub>–**PtL**<sub>3</sub>) is frequently used for studying their binding mechanism to CT-DNA. It is also noted that the studied Pt(II) C<sup>N</sup>C

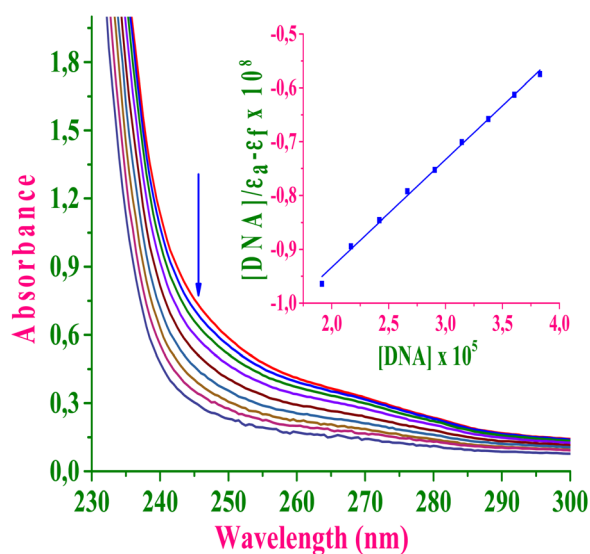


Fig. 6 Absorption spectra of **PtL**<sub>1</sub> (48  $\mu M$ ) in 5 mM Tris–HCl/50 mM buffer at pH 7.2 upon addition of CT-DNA (0–40  $\mu M$ ). The arrow shows the change in absorbance upon increasing the CT-DNA concentration. Inset: Wolfe–Shimer plot of [CT-DNA] versus [DNA]/( $\epsilon_a - \epsilon_f$ ).

Table 2 Binding constants and quenching constants for Pt(II) C<sup>N</sup>C pincer complexes (**PtL**<sub>1</sub>, **PtL**<sub>2</sub>, and **PtL**<sub>3</sub>) with CT-DNA

Complex	UV titration $K_b \times 10^{-4}, M^{-1}$	Fluorescence EtBr exchange titration				
		$K_{sv} \times 10^{-3}, M^{-1}$	$K_{app} \times 10^{-5}, M^{-1}$	$k_q \times 10^{-11}, M^{-1} s^{-1}$	$K_F \times 10^{-4}, M^{-1}$	$n$
<b>PtL</b> <sub>1</sub>	1.50 ± 0.14	6.52 ± 0.10	3.52 ± 0.25	2.83 ± 0.31	1.28 ± 0.10	0.97 ± 0.02
<b>PtL</b> <sub>2</sub>	1.15 ± 0.08	3.73 ± 0.07	2.78 ± 0.21	1.62 ± 0.23	0.55 ± 0.08	0.94 ± 0.06
<b>PtL</b> <sub>3</sub>	0.68 ± 0.03	1.86 ± 0.04	1.21 ± 0.17	0.81 ± 0.16	0.35 ± 0.05	0.92 ± 0.03



pincer complex does not show any significant fluorescence emission in the monitored range either in the absence or presence of CT-DNA when excited at 510 nm. Furthermore, the addition of **PtL<sub>1</sub>**–**PtL<sub>3</sub>** to the EtBr solution did not quench the EtBr fluorescence emission, nor did new peaks appear in the spectra, indicating that the complexes did not bind to EtBr. The addition of increasing amounts of each Pt(II) C<sup>^</sup>N<sup>^</sup>C pincer complex to the fixed concentration of EtBr + CT-DNA adduct resulted in a significant decrease in the intensity of the 596 nm band, which indicated that the studied compounds were able to displace bound EB from CT-DNA. Therefore, complexes, **PtL<sub>1</sub>**–**PtL<sub>3</sub>** can displace EtBr from its adduct with CT-DNA, as supported by the spectral changes shown in Fig. 6. It implies that the interaction between the complexes and CT-DNA changes the emission states of the EtBr + CT-DNA adduct. It is noteworthy that the fluorescence intensities were corrected for the absorption of excitation and emitted light according to simple correction factor eqn (11).

Further, in all titrations, the fluorescence emission intensity was quenched with a notable bathochromic (red) shift on each addition of complex to 20.0  $\mu\text{M}$  of a fixed concentration of EtBr bounded to CT-DNA (refer to Fig. 7a for the quenching of the EtBr–CT-DNA emission by **PtL<sub>1</sub>** for representative and also see Fig. S22a and S23a (ESI<sup>†</sup>), for changes that occur on the displacement of EtBr from the base pair of CT-DNA by the other two complexes). The quenching data were fitted to the Stern–Volmer formula (eqn (7)), and linear plots of  $I_0/I$  versus  $[Q]$  gave the Stern–Volmer quenching constant ( $K_{\text{SV}}$ ) values ( $6.52$ – $1.86 \times 10^3 \text{ M}^{-1}$ ), which are summarized in Table 2. A representative straight-line plot for **PtL<sub>1</sub>** is given in Fig. 7b, and the plots for **PtL<sub>2</sub>** and **PtL<sub>3</sub>** are given in Fig. S22b and S23b (ESI<sup>†</sup>), respectively. The quenching constants were calculated from eqn (8)

and their magnitudes are in the range of  $10^3 \text{ M}^{-1}$ , suggesting that the Pt(II) C<sup>^</sup>N<sup>^</sup>C pincer complexes can competitively exchange EtBr off the DNA medium possibly through partial intercalation or groove bindings to the CT-DNA.<sup>65</sup> The apparent binding constant  $K_{\text{app}}$  was determined from eqn (9), and the values are in the range of  $3.5$ – $1.2 \times 10^5 \text{ M}^{-1}$ . However, these values are less than the binding constants of the classical intercalators<sup>66</sup> and metallo-intercalators<sup>67</sup> (magnitude of  $10^7 \text{ M}^{-1}$ ). Since these chloro complexes are neutral, intercalative interactions can be ruled out and the observed quenching of CT-DNA–EtBr is likely due to groove binding. The bimolecular quenching rate constant ( $k_q$ ) values were also computed using the Stern–Volmer formula (eqn (10)), and the values are in the range of  $2.8$ – $0.8 \times 10^{11} \text{ M}^{-1} \text{ s}^{-1}$  (refer to Table 2). These are higher than the maximum possible range of values for biopolymeric fluorescence quenchers ( $2.0 \times 10^{10} \text{ M}^{-1} \text{ s}^{-1}$ ), suggesting that EtBr was exchanged statically from CT-DNA rather than dynamically.<sup>68</sup> Scatchard plots also gave the binding constant  $K_F$ , and the number of binding sites ‘ $n$ ’ were determined from the Scatchard formula (eqn (11)). A typical linear plot of  $\log(I_0 - I)/I$  versus  $[Q]$  for complex **PtL<sub>1</sub>** is shown in Fig. 7c, and the plots for **PtL<sub>2</sub>** and **PtL<sub>3</sub>** are given in Fig. S22c and S23c (ESI<sup>†</sup>), respectively. The magnitude and the order of the binding constants are in line with their Stern–Volmer quenching constant,  $K_{\text{SV}}$ . As shown by the trend in the magnitude of the binding and quenching values presented in Table 2, **PtL<sub>1</sub>** had the highest affinities for CT-DNA, and the increasing order of their binding ability is **PtL<sub>3</sub>** < **PtL<sub>2</sub>** < **PtL<sub>1</sub>**. Moreover, the results are in excellent agreement with data obtained from the UV-Vis spectral studies, signifying that **PtL<sub>1</sub>**–**PtL<sub>3</sub>** favour non-covalent groove binding interactions with CT-DNA.

**Cyclic voltammetry titrations of **PtL<sub>1</sub>**–**PtL<sub>3</sub>** by CT-DNA.** Cyclic voltammetry is a technique that can complement the spectroscopic

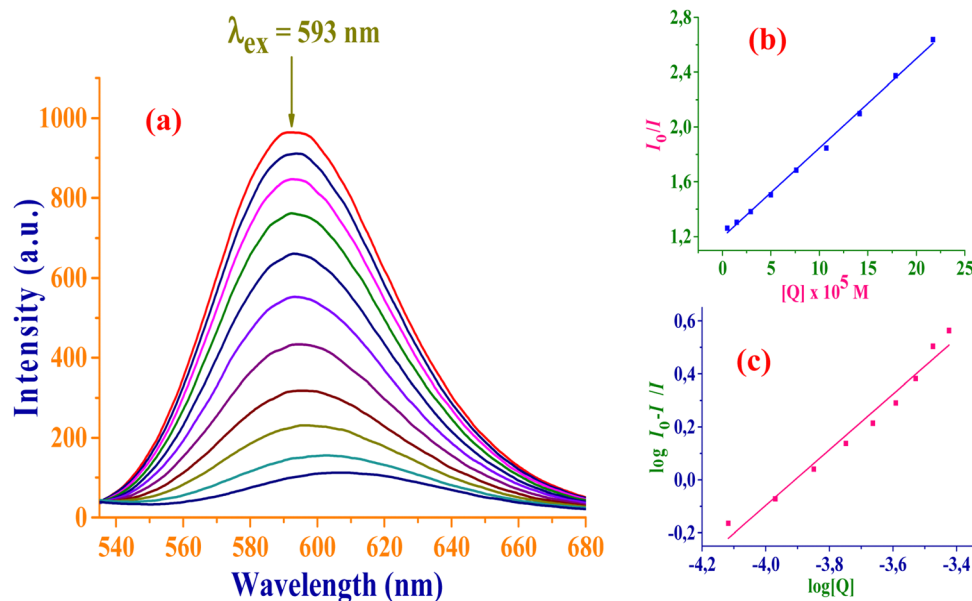


Fig. 7 (a) Fluorescence emission spectra of EtBr bounded to CT-DNA in the presence of **PtL<sub>1</sub>**: [EtBr] = 20.0  $\mu\text{M}$ , [CT-DNA] = 20.0  $\mu\text{M}$  and [**PtL<sub>1</sub>**] = 0–150  $\mu\text{M}$ . The arrow shows the intensity changes upon increasing the **PtL<sub>1</sub>** complex concentration. (b) Stern–Volmer plot of  $I_0/I$  versus  $[Q]$  and (c) Scatchard plot of  $\log(I_0 - I)/I$  versus  $\log[Q]$ .



monitoring of physicochemical changes, particularly metallo-DNA intercalations. Some mixtures of DNA-complex adducts have intrinsically weak absorption bands or overlapping bands with those of individual reactants. Fig. 8 depicts the CVs of the  $\text{PtL}_1$  complex (1.0 mM) in the presence of different concentrations of CT-DNA ranging from 15 to 75  $\mu\text{M}$  in a 1.0 mM phosphate buffer (PBS), pH 7.2, while CVs for  $\text{PtL}_1\text{--PtL}_3$ , are shown in Fig. S24a and b (ESI $^\dagger$ ). The addition of increasing amounts of CT-DNA to  $\text{PtL}_1$  or its analogues did not result in new redox peaks. However, the peak current of all the peaks decreased significantly, suggesting the existence of an interaction that forms an equilibrium-dependent adduct between  $\text{PtL}_1$  and CT-DNA that decreases the concentration of CT-DNA or the unbound  $\text{Pt(II)}$  C $^\wedge$ N $^\wedge$ C pincer complex at the electrode surface. This decrease in peak current ( $I_c$ ) over CT-DNA concentration can be used to determine estimate parameters that relate to the strength of the interactions such as binding constants or probing the binding modes/mechanisms (hydrophobic: groove or intercalative binding *versus* electrostatic interactions). As shown in the CVs, there was a slight shift in the reduction peak towards positive potentials,  $E_{pc}$ , upon the addition of increasing concentrations of CT-DNA (for CVs of  $\text{PtL}_1$ , see Fig. 8, and for  $\text{PtL}_1\text{--PtL}_3$ , Fig. S24 and Table S3, ESI $^\dagger$ ). The data indicate that binding onto DNA by  $\text{PtL}_1\text{--PtL}_3$  occurs more by partial intercalation and weak groove binding. Electrostatic binding is ruled out, given that the *cis*-coordinated carbenes make the Pt centres of the complexes electrophilic and are thus repelled by the anionic phosphate backbone of DNA. Moreover, the latter would result in shifts of  $E_{pc}$  potentials as the concentration of DNA was increased.<sup>69</sup> Groove binding causes slight drifts to less positive values or no shift in the potential peak,<sup>68</sup> as observed in Fig. 8.

Thus, these complexes partly intercalate and also loosely groove bind to DNA<sup>70</sup> while the only mode of interaction left is the groove binding. Thus, the interactions between  $\text{PtL}_1\text{--PtL}_3$  and CT-DNA are non-intercalation interactive groove binding,<sup>68,71,72</sup> as observed from their spectroscopic titration data. In addition, the decrease in the peak current with the increase in the

concentrations of CT-DNA shows that  $\text{PtL}_1\text{--PtL}_3$  interacts with CT-DNA in a concentration-dependent manner.

The variation in the reduction peak current ( $I_{pc}$ ) over CT-DNA concentration can be exploited for the determination of binding parameters. The binding constant  $K$  was calculated from both the intercept of the plot of  $\log(1/[\text{CT-DNA}])$  *versus*  $\log(I/(I_0 - I))$ , according to eqn (3).<sup>73</sup> The values of 4.18, 1.22 and  $0.10 \times 10^3 \text{ M}^{-1}$  for  $\text{PtL}_1\text{--PtL}_3$ , respectively were obtained and they were in the same trending order as those obtained from spectroscopic results. The representative linear plots of  $\log(1/[\text{CT-DNA}])$  *versus*  $\log(I/(I_0 - I))$  are given in the inset of Fig. 8 for the complex  $\text{PtL}_1$ , while for the other two complexes, the plots are given as insets in Fig. S24a and b (ESI $^\dagger$ ). Thus, the change in the Gibbs free energy,  $\Delta G_b$ , for the binding interactions of  $\text{PtL}_1\text{--PtL}_3$  with CT-DNA was also computed using eqn (6) and negative values of  $-21.34$ ,  $-18.18$  and  $-11.84 \text{ kJ mol}^{-1}$  for  $\text{PtL}_1\text{--PtL}_3$  were obtained, respectively. The negative values of  $\Delta G$  indicate the spontaneity of binding of  $\text{PtL}_1\text{--PtL}_3$  with CT-DNA as well and the decreasing order of magnitude is well corroborated with their binding order and thus their reactivity trend, *i.e.*,  $\text{PtL}_1 > \text{PtL}_2 > \text{PtL}_3$ .

**Viscometric studies.** Viscosity measurements of DNA solution mixtures provide unambiguous data that correlate with the helical structural changes of DNA induced by its interactions with other molecules. For example, small intercalating molecules cause the DNA helix to elongate as its base pairs get separated to accommodate the intercalating molecule. This leads to increased DNA viscosity. Non-classical intercalators cause a bend or kinks in the DNA helix, which reduces its effective length and thus maintains its viscosity to remain almost constant, or in some cases, a reduction.<sup>74</sup> When the relative concentration of  $\text{PtL}_1\text{--PtL}_3$  in CT-DNA (5.0 mM Tris-HCl buffer, pH 7.2) is increased (1.0–6.0 mM), the viscosity of the solutions remained almost constant, as shown in Fig. S25 (ESI $^\dagger$ ) (relative viscosities were computed using eqn (4)). However, the viscosity of CT-DNA solutions increased dramatically when the concentration of a classical intercalator like EtBr interacted (refer to Fig. S25, ESI $^\dagger$ ). Thus, due to the marked dissimilarity in the viscosity trends for the  $\text{Pt(II)}$  C $^\wedge$ N $^\wedge$ C pincer complexes compared to that of EtBr (a DNA intercalator), and hence, the changes in the helical structure of the DNA, the interactions of the complexes with CT-DNA are more likely to be due to groove-binding rather than classical intercalation which is consistent with our foregoing postulation. Further, the trend in the viscosity is similar to that observed for the solutions of DNA-distamycin (a well-known non-electrostatic DNA groove binder).<sup>75,76</sup> Thus, the studied  $\text{Pt(II)}$  C $^\wedge$ N $^\wedge$ C pincer complexes bind onto the hydrophobic pockets of the CT-DNA strongly *via* groove binding mode of interactions.

### BSA interactions

**UV-Visible absorption studies.** Interactions between metal complexes (guest) and transporter proteins such as BSA can be studied by monitoring UV-Vis absorption spectral (decrease/increase intensity of shift in the frequency of absorption) changes corresponding to either the reactants or the formation of the BSA-guest adducts. BSA has two main absorption bands including (i) one weak centred at 280 nm, where only the

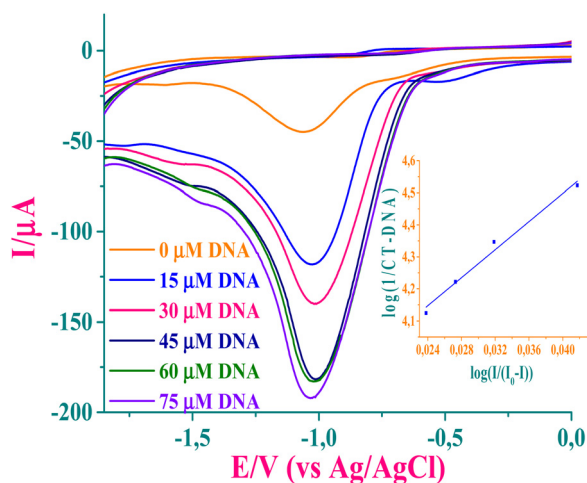


Fig. 8 Cyclic voltammograms of 1.0 mM of  $\text{PtL}_1$  without and with CT-DNA at  $100 \text{ mV s}^{-1}$ .





aromatic side chains of the proteins absorb, and (ii) one strong band within the range 210–230 nm, where aromatic amino acids such as histidine, cysteine and their peptide combinations absorb collectively. Thus, stacked absorption spectra of 10  $\mu\text{M}$  BSA in the absence and presence of a fixed concentration (5  $\mu\text{M}$ ) of  $\text{PtL}_1$ – $\text{PtL}_3$  were recorded, as illustrated in Fig. S26 (ESI $^\dagger$ ). The absorption intensity of BSA increases upon the addition of complexes. The hyperchromism indicates that there is a strong associative interaction between the complexes' ligand groups with the aromatic amino acid residues of BSA that cause the conformational changes in BSA as a result of a change dipolar microenvironment of the proximity amino acids of BSA.<sup>77</sup> These spectral changes can also be used to distinguish if the quenching mechanism is either static or dynamic. In dynamic quenching, the fluorophore and the quencher come into contact during the transient existence of the excited state, whereas in static quenching,<sup>78</sup> the fluorophore-quencher complex forms in the ground state. The observed spectral changes imply that the interactions between BSA and complexes  $\text{PtL}_1$ – $\text{PtL}_3$  are ground-state derived and thus static rather than dynamic.

**Fluorescence quenching studies.** The tryptophan fluorescence emission quenching titrations by  $\text{PtL}_1$ – $\text{PtL}_3$  were performed to gain further insights into the binding affinities of  $\text{PtL}_1$ – $\text{PtL}_3$  with BSA. The addition of complexes  $\text{PtL}_1$ – $\text{PtL}_3$  (0–20  $\mu\text{M}$ ) into a BSA solution (24.8  $\mu\text{M}$ ) resulted in a quenching of its fluorescence emission band at  $\lambda_{\text{em}} = 346$  nm, and the fluorescence intensities were corrected according to eqn (11). A decrease in emission intensity at  $\lambda_{\text{em}}$  (346 nm) of BSA when  $[\text{PtL}_1/\text{PtL}_2/\text{PtL}_3]$  is increased indicates associative interactions between the BSA and the quenchers. Typical overlays of BSA emission spectra are depicted in Fig. 9a for  $\text{PtL}_1$ , also refer to Fig. S27a and S28a (ESI $^\dagger$ ), for other complexes. The change in intensity data

with successive addition of each complex fitted well to the Stern–Volmer formula (eqn (8)), which gives the Stern–Volmer quenching constant  $K_{\text{sv}}$  from the slopes of the linear plots of  $I_0/I$  versus  $[Q]$ . The representative linear Stern–Volmer plots for  $\text{PtL}_1$  are given in Fig. 9b, and refer to Fig. S27b and S28b (ESI $^\dagger$ ), for the other two complexes. The bimolecular quenching rate constant,  $k_q$ , was also computed from eqn (10) and the values are presented in Table 3. The data were fitted to the Scatchard formula (eqn (11)). The typical linear Scatchard plot for  $\text{PtL}_1$  is given in Fig. 9c while for the other complexes, refer to Fig. S27c and S28c (ESI $^\dagger$ ). These plots were used to determine the binding constants,  $K_F$ , and the number of binding sites,  $n$ , and the results are summarized in Table 3 and Fig. S27c and S28c (ESI $^\dagger$ ). The magnitudes of  $K_F$  values ( $10^3 \text{ M}^{-1}$ ) indicate moderate to strong binding of the complexes. The quenching of the tryptophan emission suggests that the interactions are hydrophobic since the former is located in the hydrophobic domains of BSA.<sup>79</sup> The analyzed  $n$  values for all the complexes are approximately 1, strongly suggesting that the complexes are bound to BSA as 1:1 adducts. The data presented in Table 3 ( $K_{\text{sv}}$ ,  $k_q$  and  $K_F$ ) confirm that the complex,  $\text{PtL}_1$ , has the highest BSA (proteins) binding strength followed by  $\text{PtL}_2$  and  $\text{PtL}_3$ , in the increasing order of  $\text{PtL}_3 < \text{PtL}_2 < \text{PtL}_1$ .

Thus, the data from the interaction studies (Tables 2 and 3) indicate that complexes  $\text{PtL}_1$ – $\text{PtL}_3$  have moderate binding affinities to both CT-DNA and BSA. The binding abilities (from both UV-vis and fluorescence studies) of the studied complexes with CT-DNA suggest the groove binding mode of interactions, while the hydrophobic interactions are responsible for the strong interaction of BSA with  $\text{PtL}_1$ – $\text{PtL}_3$  and the binding abilities of the complexes follow the order of  $\text{PtL}_1 > \text{PtL}_2 > \text{PtL}_3$ . Overall, the rate of chloride substitution with S-donor nucleophiles follows

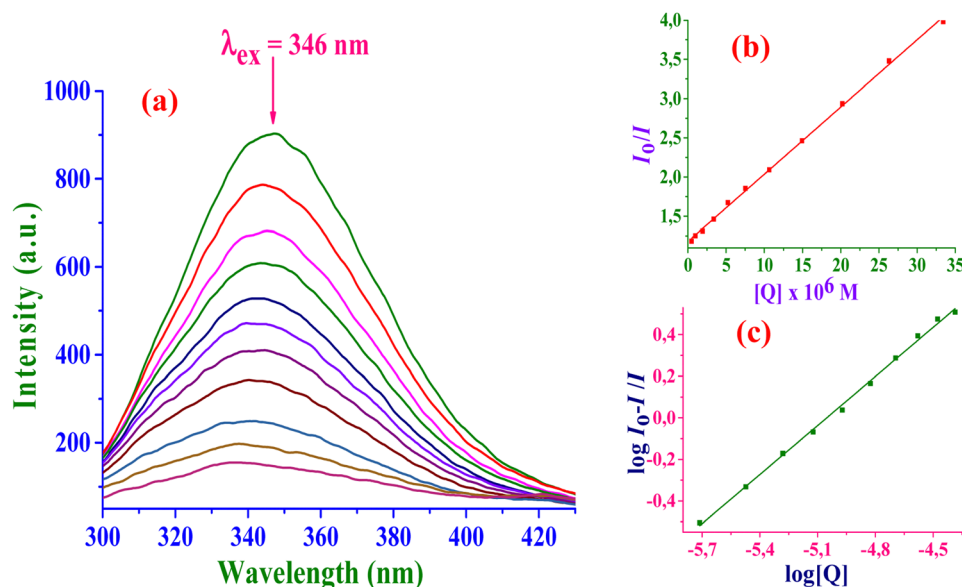


Fig. 9 (a) Fluorescence emission spectra of BSA in the absence and presence of  $\text{PtL}_1$ :  $[\text{BSA}] = 24.8 \mu\text{M}$  and  $[\text{PtL}_1] = 0$ – $20 \mu\text{M}$ . The arrow shows the intensity changes upon increasing the  $\text{PtL}_1$  complex concentration. (b) Stern–Volmer plot of  $I_0/I$  versus  $[Q]$  and (c) Scatchard plot of  $\log[(I_0 - I)/I]$  versus  $\log[Q]$ .



**Table 3** Binding constant, quenching constants and binding sites for the Pt(II) C<sup>^</sup>N<sup>^</sup>C pincer complexes with BSA

Complex	$K_{sv} \times 10^{-4}$ , $M^{-1}$	$k_q \times 10^{-12}$ , $M^{-1} s^{-1}$	$K_F \times 10^{-3}$ , $M^{-1}$	$n$
PtL <sub>1</sub>	8.57 ± 0.13	8.57 ± 0.16	9.37 ± 0.09	1.00 ± 0.03
PtL <sub>2</sub>	2.87 ± 0.08	2.87 ± 0.11	1.83 ± 0.05	1.00 ± 0.04
PtL <sub>3</sub>	0.98 ± 0.04	0.98 ± 0.05	0.30 ± 0.03	0.09 ± 0.02

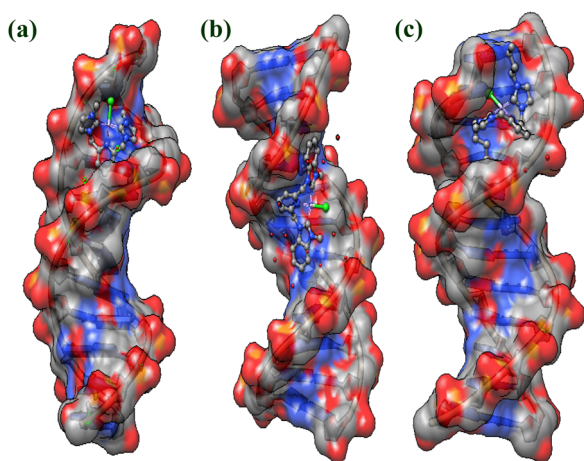
the same order of reactivity, thus the binding interaction and electrochemical studies are well corroborated by kinetic results.

### Molecular docking studies

**Docking with B-DNA.** The molecular docking technique is an attractive scaffold to understand the metal complex-DNA interactions in rational drug design and discovery, as well as in the mechanistic study.<sup>80</sup> Molecular modeling allows flexibility within the ligand to be modeled and can utilize more detailed molecular mechanism to calculate the energy of the ligand in the context of the putative active site. In simulations, PtL<sub>1</sub>–PtL<sub>3</sub> were docked onto B-DNA to attain different conformations to predict the binding mode of complexes with the DNA duplex sequence, which provides an energetically favourable docked pose shown in Fig. 10. The minimum energy docked pose results show that the complexes PtL<sub>1</sub>–PtL<sub>3</sub> interact with the DNA helix involving outside edge stacking interactions with the oxygen atom of the phosphate backbone of DNA. In this model, it is indicated that the studied complexes fit into the curved contour of the targeted DNA in the groove and are situated within the GC-rich region. This leads to van der Waals and hydrophobic interactions with DNA functional groups that define the stability of the groove adduct.<sup>81,82</sup> In the groove binding, PtL<sub>1</sub>–PtL<sub>3</sub> inserts between two consecutive AT base pairs, forming  $\pi$ – $\pi$  stacking interactions between the oxygen atom of the phosphate backbone of DNA base pairs, while the linker chain binds to the extended minor groove by forming simple hydrophobic interactions. The relative magnitude of the binding energy of complexes was found to be –53.71, –44.23

and –39.29 kcal mol<sup>–1</sup> for PtL<sub>1</sub>/PtL<sub>2</sub>/PtL<sub>3</sub>, respectively, which indicates the binding propensity order of the complexes with DNA. The computed  $E_{(\text{lowest energy pose})}$  values are consistent with the observed trend in binding strength from the spectroscopic (absorption and fluorescence quenching titration) and electrochemical (see Tables 2 and 3) studies, and the increasing binding order is PtL<sub>3</sub> < PtL<sub>2</sub> < PtL<sub>1</sub>. Irrespective of the absence of any net positive charge on Pt(II) C<sup>^</sup>N<sup>^</sup>C pincer complexes, the negative value of the binding energy indicated a higher binding potential of the studied complexes with DNA. The more negative the relative binding energy values, the greater the binding potential between DNA and complexes, which correlated well with the experimental DNA binding studies. Thus, we conclude that there is a mutual coherence between spectroscopic techniques and molecular docking techniques, which can substantiate our experimental results about the mode of interaction of PtL<sub>1</sub>–PtL<sub>3</sub> with DNA and provide further evidence of groove binding interactions.

**Docking with BSA.** Molecular docking experiments of studied PtL<sub>1</sub>–PtL<sub>3</sub> were performed to identify the preferential binding sites in BSA and for a better understanding of the mechanism of action. Serum albumin as the most abundant carrier protein comprises three  $\alpha$ -helical homologous domains (I, II, and III), and each domain contains two subdomains (A and B). Fig. 11 and Fig. S29a and b (ESI<sup>†</sup>), show that the docked conformations of PtL<sub>1</sub>–PtL<sub>3</sub> lie in the interdomain region called the protein cleft (PC) separating subdomains IA, IB, and IIA on one side and subdomains IIB, IIIA and IIIB on the other side and supported by dipolar hydrogen bonding as well as short contacts *via* van der Waals interactions.<sup>83,84</sup> All the three complexes (PtL<sub>1</sub>–PtL<sub>3</sub>) insert into the upper PC surrounded by charged amino residues such as Leu 112, Leu 115, Ile 189, Leu 189, His 145, Asp 111, Lys 114, Arg 458 and Pro 110 to PtL<sub>1</sub>, (Fig. 11) Leu 112, Leu 189, His 145, Arg 144, Glu 186, Arg 458, Glu 424, Thr 190, Ser 109, Asp 111, Ser 192 and Ala 193 to PtL<sub>2</sub>, (inset of Fig. S29a, ESI<sup>†</sup>) Ile 141, Ile 115, Leu 189,

**Fig. 10** Docking poses, illustrating the non-covalent interactions of PtL<sub>1</sub> (a), PtL<sub>2</sub> (b) and PtL<sub>3</sub> (c) with the B-DNA duplex.**Fig. 11** Lowest binding free energy conformers were obtained between PtL<sub>1</sub> and BSA.

Leu 112, Val 188, Arg 185, Lys 114, Asp 111, Arg 144, Glu 424, Arg 458, His 145, Ser 109 and Pro 110 to **PtL<sub>3</sub>** (inset of Fig. S29b, ESI†), respectively. Electrostatic and van der Waals interactions play a key role in the binding of **PtL<sub>1</sub>–PtL<sub>3</sub>** at the PC<sub>upper</sub> pocket, which is consistent with a thermodynamic interpretation. The computed binding free energies were found to be  $-54.94$ ,  $-38.59$  and  $-34.67$  kJ mol<sup>-1</sup> for **PtL<sub>1</sub>**, **PtL<sub>2</sub>** and **PtL<sub>3</sub>** respectively. The relatively large negative binding energy value for **PtL<sub>1</sub>** indicates that the PC cavity and the neighboring residues stabilize the metal complex by sturdier electrostatic interactions. The other two complexes are relatively voluminous and show smaller binding energies with BSA. Thus, the binding abilities of the studied Pt(II) C<sup>N</sup>C pincer complexes well corroborate with the one obtained from thermodynamic parameter analysis, and the order is as follows: **PtL<sub>1</sub>** > **PtL<sub>2</sub>** > **PtL<sub>3</sub>**. Moreover, conformational changes were not observed for **PtL<sub>1</sub>–PtL<sub>3</sub>** indicating that the substituents in the imidazole rings of the carbenes do not change the orientation of the molecules in the BSA protein. Thus, correlating the values determined by the Stern–Volmer quenching and binding constants and molecular docking, it could be seen that both experiments show that there were more pronounced interactions of tryptophan with complexes. It is believed that these increased interactions occur because of the distorted square planar-geometry of these Pt(II) compounds.

## Conclusions

Substitution kinetics demonstrated that the reactivity of the six-membered Pt(II) C<sup>N</sup>C pincer complexes (**PtL<sub>2</sub>** and **PtL<sub>3</sub>**) is driven by electronic and steric factors, respectively when compared to **PtL<sub>1</sub>**, and the reactivity order is as follows: **PtL<sub>1</sub>** > **PtL<sub>2</sub>** > **PtL<sub>3</sub>**. Extended  $\pi$ -conjugation and *N*-butyl arms on the bis(3-methylimidazolium-1-yl)pyridine ligand moiety facilitate the enhanced  $\sigma$ -inductive effect and impart steric hindrance to the approaching nucleophiles, respectively. The extended  $\pi$ -surface on **PtL<sub>2</sub>** further stabilizes the complex towards substitution *via* annular nitrogen atoms of the imidazole, while in **PtL<sub>3</sub>**, the shorter *N*-methine hydrogen distance Cl $\cdots$ H constrains the free spaces around the Pt(II) metal centre and thus restricts the approaching nucleophiles, which lead to reduced reactivity. Besides, the rise in  $E_{\text{LUMO}}$  signals the dis-stabilization of  $\pi^*$  orbitals of the complex. This makes the complex a poor  $\pi$ -acceptor, leading to lower reactivity. Moreover, no electronic evidence was linked to the *N*-alkyl substituent arms leaving the steric influence by the substituent arms of the *cis*-coordinated carbenes as the main factor for the least substitution reactivity observed for the **PtL<sub>3</sub>** complex.

The spectroscopic and CV titrations of **PtL<sub>1</sub>–PtL<sub>3</sub>** revealed that all three complexes showed notable binding affinities towards both CT-DNA and BSA. Complexes bind to the CT-DNA helix *via* the groove binding mode of interaction with no conformational changes or unwinding of the double helix, whereas they bind in the upper protein cleft of BSA, stabilized by the charges on the residues. The mechanism of

CT-DNA–EtBr or BSA interactions (as monitored *via* emission quenching titrations) with complexes **PtL<sub>1</sub>–PtL<sub>3</sub>** was considered static in which the latter quenchers occupied single binding sites. A negative free energy change ( $\Delta G < 0$ ) emphasizes the spontaneity of the binding process. Electrochemical studies further highlighted an EC mechanism *via* a typical diffusion-controlled electrode process. The results of molecular docking calculations of complexes showed the predominance of non-intercalative interactions in the minor groove of the B-DNA sequence, while they preferred the PC<sub>upper</sub> binding sites of the BSA where they are surrounded mostly by charged protein residues.

## Data availability

Raw data were generated at the University of KwaZulu-Natal, South Africa. The authors confirm that the data supporting the findings of this study are available within the article [and/or] its ESI.†

## Conflicts of interest

There are no conflicts to declare.

## Acknowledgements

The authors greatly acknowledge the University of KwaZulu-Natal, South Africa for providing financial support to the work.

## References

- 1 C. J. Moulton and B. L. Shaw, *J. Chem. Soc., Dalton Trans.*, 1976, **11**, 1020–1024.
- 2 G. van Koton, K. Timmer, J. G. Noltes and A. L. Spek, *J. Chem. Soc., Chem. Commun.*, 1978, **6**, 250–252.
- 3 L. González-Sebastián and D. Morales-Morales, *J. Org. Chem.*, 2019, **893**, 39–51.
- 4 H. W. Wanzlick and H. J. Schönherr, *Angew. Chem., Int. Ed. Engl.*, 1968, **7**, 141–142.
- 5 K. Öfele, *J. Org. Chem.*, 1968, **12**, 42–43.
- 6 M. Alcarazo, T. Stork, A. Anoop, W. Thiel and A. Fürstner, *Angew. Chem., Int. Ed.*, 2010, **49**, 2542–2546.
- 7 V. Nair, S. Bindu and V. Sreekumar, *Angew. Chem., Int. Ed.*, 2004, **43**, 5130–5135.
- 8 J. S. Owen, J. A. Labinger and J. E. Bercaw, *J. Am. Chem. Soc.*, 2004, **126**, 8247–8255.
- 9 T. W. Hudnall and C. W. Bielawski, *J. Am. Chem. Soc.*, 2009, **131**, 16039–16041.
- 10 T. Scherg, S. K. Schneider, G. D. Frey, J. Schwarz, E. Herdtweck and W. A. Herrmann, *Synlett*, 2006, 2894–2907.
- 11 M. Albrecht, J. R. Miecznikowski, A. Samuel, J. W. Faller and R. H. Crabtree, *Organometallics*, 2002, **21**, 3596–3604.
- 12 L. Oehninger, R. Rubbiani and I. Ott, *Dalton Trans.*, 2013, **42**, 3269–3284.
- 13 A. L. Noffke, A. Habtemariam, A. M. Pizarro and P. J. Sadler, *Chem. Commun.*, 2012, **48**, 5219–5246.





- 14 J. K. Muenzner, T. Rehm, B. Biersack, A. Casini, I. A. de Graaf, P. Worawutputtapong, A. Noor, R. Kempe, V. Brabec and J. Kasparkova, *J. Med. Chem.*, 2015, **58**, 6283–6292.
- 15 W. C. Schiessl, N. K. Summa, C. F. Weber, S. Gubo, C. Dücker-Benfer, R. Puchta, N. J. van Eikema Hommes and R. van Eldik, *Zeitschrift für anorganische und allgemeine Chemie*, 2005, **631**, 2812–2819.
- 16 R. A. Haque, P. O. Asekunowo, S. Budagumpi and L. Shao, *Eur. J. Inorg. Chem.*, 2015, 3169–3181.
- 17 K. Mutua, R. Bellam, D. Jaganyi and A. Mambanda, *J. Coord. Chem.*, 2019, **72**, 2931–2956.
- 18 *OriginPro 9.1*, OriginLab Corporation, One Roundhouse, Plaza, suite 303, Northampton, MA 01060, USA.
- 19 M. Frisch, G. Trucks, H. B. Schlegel, G. Scuseria, M. Robb, J. Cheeseman, G. Scalmani, V. Barone, B. Mennucci and G. Petersson *et al.*, *Gaussian 09*, Gaussian Inc, Wallingford CT, 2009.
- 20 R. O. Omondi, R. Bellam, S. O. Ojwach, D. Jaganyi and A. A. Fatokun, *J. Inorg. Biochem.*, 2020, **210**, 111156.
- 21 J. Marmur, *J. Mol. Biol.*, 1961, **3**, 208–IN201.
- 22 A. Pyle, J. Rehmann, R. Meshoyrer, C. Kumar, N. Turro and J. K. Barton, *J. Am. Chem. Soc.*, 1989, **111**, 3051–3058.
- 23 A. Paul, H. Puschmann and S. C. Manna, *Polyhedron*, 2018, **155**, 447–456.
- 24 F. J. Meyer-Almes and D. Porschke, *Biochem.*, 1993, **32**, 4246–4253.
- 25 O. Stern and M. Volmer, *Phys. Z.*, 1919, **20**, 183–188.
- 26 D. P. Heller and C. L. Greenstock, *Biophys. Chem.*, 1994, **50**, 305–312.
- 27 M. Lee, A. L. Rhodes, M. D. Wyatt, S. Forrow and J. A. Hartley, *Biochem.*, 1993, **32**, 4237–4245.
- 28 J. R. Lakowicz, *Principles of fluorescence spectroscopy*, Springer Science & Business Media, 2013.
- 29 E. Alarcon, A. Aspée, M. Gonzalez-Bejar, A. Edwards, E. Lissi and J. Scaiano, *Photochem. Photobiol. Sci.*, 2010, **9**, 861–869.
- 30 X. Zhao, R. Liu, Z. Chi, Y. Teng and P. Qin, *J. Phys. Chem. B*, 2010, **114**, 5625–5631.
- 31 C. Parker and W. Rees, *Anal.*, 1962, **87**, 83–111.
- 32 M. Puchalski, M. Morra and R. Von Wandruszka, *Fresenius' J. Anal. Chem.*, 1991, **340**, 341–344.
- 33 I. M. Wekesa and D. Jaganyi, *Dalton Trans.*, 2014, **43**, 2549–2558.
- 34 B. Petrovic, Z. D. Bugarcic, A. Dees, I. I. Burmazovic, F. W. Heinemann, R. Puchta, S. N. Steinmann, C. Corminboeuf and R. van Eldik, *Inorg. Chem.*, 2012, **51**, 1516–1529.
- 35 R. O. Omondi, N. R. S. Sibuyi, A. O. Fadaka, M. Meyer, D. Jaganyi and S. O. Ojwach, *Dalton Trans.*, 2021, **50**, 8127–8143.
- 36 T. Soldatovic and Z. D. Bugarcic, *J. Inorg. Biochem.*, 2005, **99**, 1472–1479.
- 37 R. Bellam and N. R. Anipindi, *Transition Met. Chem.*, 2014, **39**, 311–326.
- 38 R. Bellam, D. Jaganyi, A. Mambanda and R. Robinson, *New J. Chem.*, 2018, **42**, 12557–12569.
- 39 R. Bellam, N. R. Anipindi and D. Jaganyi, *J. Mol. Liq.*, 2018, **258**, 57–65.
- 40 R. Bellam, S. Sivamadhavi, S. Ramakrishna, A. Mambanda, D. Jaganyi and N. R. Anipindi, *J. Coord. Chem.*, 2017, **70**, 1893–1909.
- 41 J. Huang, E. D. Stevens, S. P. Nolan and J. L. Petersen, *J. Am. Chem. Soc.*, 1999, **121**, 2674–2678.
- 42 M. Regitz, *Angew. Chem., Int. Ed. Engl.*, 1996, **35**, 725–728.
- 43 A. C. Hillier, W. J. Sommer, B. S. Yong, J. L. Petersen, L. Cavallo and S. P. Nolan, *Organomet.*, 2003, **22**, 4322–4326.
- 44 T. Papo, D. Jaganyi and A. Mambanda, *J. Coord. Chem.*, 2024, **77**, 638–652.
- 45 R. Bellam and D. Jaganyi, *Int. J. Chem. Kinet.*, 2017, **49**, 182–196.
- 46 D. O. Onunga, R. Bellam, G. K. Mutua, M. Sitati, M. D. BalaKumaran, D. Jaganyi and A. Mambanda, *J. Inorg. Biochem.*, 2020, **213**, 111261.
- 47 D. Bourissou, O. Guerret, F. P. Gabbai and G. Bertrand, *Chem. Rev.*, 2000, **100**, 39–92.
- 48 H. Jacobsen, A. Correa, A. Poater, C. Costabile and L. Cavallo, *Coord. Chem. Rev.*, 2009, **253**, 687–703.
- 49 D. Jaganyi, D. Reddy, J. A. Gertenbach, A. Hofmann and R. van Eldik, *Dalton Trans.*, 2004, 299–304.
- 50 A. Juris, F. Barigelletti, V. Balzani, P. Belser and A. Von Zelewsky, *Inorg. Chem.*, 1985, **24**, 202–206.
- 51 A. Jayamani, R. Bellam, G. Gopu, S. O. Ojwach and N. Sengottuvelan, *Polyhedron*, 2018, **156**, 138–149.
- 52 R. G. Parr, L. v Szentpály and S. Liu, *J. Am. Chem. Soc.*, 1999, **121**, 1922–1924.
- 53 I. M. Wekesa and D. Jaganyi, *Dalton Trans.*, 2014, **43**, 2549–2558.
- 54 R. Bellam, D. Jaganyi, A. Mambanda, R. Robinson and M. D. BalaKumaran, *RSC Adv.*, 2019, **9**, 31877–31894.
- 55 C. Sandford, M. A. Edwards, K. J. Klunder, D. P. Hickey, M. Li, K. Barman, M. S. Sigman, H. S. White and S. D. Minter, *Chem. Sci.*, 2019, **10**, 6404–6422.
- 56 M. T. Carter, M. Rodriguez and A. J. Bard, *J. Am. Chem. Soc.*, 1989, **111**, 8901–8911.
- 57 I. Kocak, U. Yildiz, B. Coban and A. Sengul, *J. Solid State Electrochem.*, 2015, **19**, 2189–2197.
- 58 N. Martin, R. Behnisch and M. Hanack, *J. Org. Chem.*, 1989, **54**, 2563–2568.
- 59 K. Hanson, L. Roskop, P. I. Djurovich, F. Zahariev, M. S. Gordon and M. E. Thompson, *J. Am. Chem. Soc.*, 2010, **132**, 16247–16255.
- 60 T. Albrecht, K. Moth-Poulsen, J. B. Christensen, A. Guckian, T. Bjørnholm, J. G. Vos and J. Ulstrup, *Faraday Discuss.*, 2006, **131**, 265–279.
- 61 D. K. Gosser, *Cyclic voltammetry: simulation and analysis of reaction mechanisms*, VCH, New York, 1993.
- 62 Y. Zhu and C. Wang, *J. Phys. Chem. C*, 2011, **115**, 823–832.
- 63 H. Luo, Z. Shi, N. Li, Z. Gu and Q. Zhuang, *Anal. Chem.*, 2001, **73**, 915–920.
- 64 K. S. Neethu, E. Jayanthi, M. Theetharappan, S. P. Bhuvanesh Nattamai, M. A. Neelakantan and M. V. Kaveri, *Appl. Organomet. Chem.*, 2019, **33**, e4751.
- 65 J. C. Peberdy, J. Malina, S. Khalid, M. J. Hannon and A. Rodger, *J. Inorg. Biochem.*, 2007, **101**, 1937–1945.
- 66 M. Cory, D. D. McKee, J. Kagan, D. Henry and J. A. Miller, *J. Am. Chem. Soc.*, 1985, **107**, 2528–2536.





- 67 I. Mitra, S. Mukherjee, B. Misini, P. Das, S. Dasgupta, W. Linert and S. C. Moi, *New J. Chem.*, 2018, **42**, 2574–2589.
- 68 N. Maurya, K. Imtiyaz, M. M. A. Rizvi, K. M. Khedher, P. Singh and R. Patel, *RSC Adv.*, 2020, **10**, 24203–24214.
- 69 M. T. Carter and A. J. Bard, *J. Am. Chem. Soc.*, 1987, **109**, 7528–7530.
- 70 F. Jafari, S. Moradi, A. Nowroozi, K. Sadriavadi, L. Hosseinzadeh and M. Shahlaei, *New J. Chem.*, 2017, **41**, 14188–14198.
- 71 S. Z. Moradi, A. Nowroozi, K. Sadriavadi, S. Moradi, K. Mansouri, L. Hosseinzadeh and M. Shahlaei, *Int. J. Biol. Macromol.*, 2018, **114**, 40–53.
- 72 M. Rodriguez and A. J. Bard, *Anal. Chem.*, 1990, **62**, 2658–2662.
- 73 Q. Feng, N. Q. Li and Y. Y. Jiang, *Anal. Chim. Acta*, 1997, **344**, 97–104.
- 74 S. Satyanarayana, J. C. Dabrowiak and J. B. Chaires, *Biochem.*, 1993, **32**, 2573–2584.
- 75 M. P. Barrett, C. G. Gemmell and C. J. Suckling, *Pharm. Therapy.*, 2013, **139**, 12–23.
- 76 L. Lerman, *J. Mol. Biol.*, 1961, **3**, 18–IN14.
- 77 H. Polet and J. Steinhardt, *Biochem.*, 1968, **7**, 1348–1356.
- 78 R. Bellam, D. Jaganyi and R. S. Robinson, *ACS Omega*, 2022, **7**, 26226–26245.
- 79 Z. J. Cheng, H. M. Zhao, Q. Y. Xu and R. Liu, *J. Pharm. Anal.*, 2013, **3**, 257–269.
- 80 R. Esteghamat-Panah, H. Farrokhpour, H. Hadadzadeh, F. Abyar and H. A. Rudbari, *RSC Adv.*, 2016, **6**, 23913–23929.
- 81 R. Filosa, A. Peduto, S. Di Micco, P. de Caprariis, M. Festa, A. Petrella, G. Capranico and G. Bifulco, *Bioorg. Med. Chem.*, 2009, **17**, 13–24.
- 82 X. B. Fu, D. D. Liu, Y. Lin, W. Hu, Z. W. Mao and X. Y. Le, *Dalton Trans.*, 2014, **43**, 8721–8737.
- 83 I. Petitpas, C. E. Petersen, C. E. Ha, A. A. Bhattacharya, P. A. Zunszain, J. Ghuman, N. V. Bhagavan and S. Curry, *Proc. Natl. Acad. Sci. U. S. A.*, 2003, **100**, 6440–6445.
- 84 P. Ascenzi, A. Di Masi, G. Fanali and M. Fasano, *Cell Death Dis.*, 2015, **1**, 1–7.

